Emeis, K.-C., Robertson, A.H.F., Richter, C., et al., 1996
Proceedings of the Ocean Drilling Program, Initial Reports, Vol. 160

4. SITE 963[1]

Shipboard Scientific Party[2]

HOLE 963A

Date occupied: 14 March 1995

Date departed: 15 March 1995

Time on hole: 1 day, 00 hr, 15 min

Position: 37°01.938′N, 13°10.896′E

Bottom felt (drill-pipe measurement from rig floor, m): 481.0

Distance between rig floor and sea level (m): 10.5

Water depth (drill-pipe measurement from sea level, m): 470.5

Total depth (from rig floor, m): 680.4

Penetration (m): 199.4

Number of cores (including cores having no recovery): 25

Total length of cored section (m): 199.4

Total core recovered (m): 203.1

Core recovery (%): 101.9

Oldest sediment cored:
Depth (mbsf): 199.4
Nature: nannofossil clay
Earliest age: early Pleistocene
Measured velocity (km/s): 1.65

HOLE 963B

Date occupied: 15 March 1995

Date departed: 16 March 1995

Time on hole: 14 hr, 30 min

Position: 37°02.004′N, 13°10.830′E

Bottom felt (drill-pipe measurement from rig floor, m): 481.0

Distance between rig floor and sea level (m): 11.0

Water depth (drill-pipe measurement from sea level, m): 470.0

Total depth (from rig floor, m): 688.0

Penetration (m): 204.5

Number of cores (including cores having no recovery): 24

Total length of cored section (m): 204.5

Total core recovered (m): 206.2

Core recovery (%): 100.8%

Oldest sediment cored:
Depth (mbsf): 207.00
Nature: nannofossil clay
Earliest age: early Pleistocene
Measured velocity (km/s): 1.65

HOLE 963C

Date occupied: 16 March 1995

Date departed: 16 March 1995

Time on hole: 04 hr, 15 min

Position: 37°02.076′N, 13°10.758′E

Bottom felt (drill-pipe measurement from rig floor, m): 480.0

Distance between rig floor and sea level (m): 11.0

Water depth (drill-pipe measurement from sea level, m): 469.0

Total depth (from rig floor, m): 537.0

Penetration (m): 57.0

Number of cores (including cores having no recovery): 6

Total length of cored section (m): 57.0

Total core recovered (m): 57.9

Core recovery (%): 101.6

Oldest sediment cored:
Depth (mbsf): 57.00

Comments: Hole 963C was not described.

HOLE 963D

Date occupied: 16 March 1995

Date departed: 16 March 1995

Time on hole: 05 hr, 15 min

Position: 37°02.148′N, 13°10.686′E

Bottom felt (drill-pipe measurement from rig floor, m): 480.1

Distance between rig floor and sea level (m): 11.0

Water depth (drill-pipe measurement from sea level, m): 469.1

Total depth (from rig floor, m): 488.5

Penetration (m): 8.4

Number of cores (including cores having no recovery): 1

Total length of cored section (m): 8.4

Total core recovered (m): 8.4

Core recovery (%): 99.0

Oldest sediment cored:
Depth (mbsf): 8.40

Comments: Hole 963D was not described.

Principal results: Site 963 is located on the sill between the eastern and western Mediterranean sub-basins and is the westernmost location drilled during Leg 160. The seafloor at the site forms an embayment off the

[1]Emeis, K.-C., Robertson, A.H.F., Richter, C., et al., 1996. *Proc. ODP, Init. Repts.,* 160: College Station, TX (Ocean Drilling Program).
[2]Shipboard Scientific Party is given in the list preceding the Table of Contents.

Pantelleria, Linosa, and Malta grabens in the Strait of Sicily, which channel the flow of Mediterranean Intermediate Water from the eastern to the western Mediterranean basins.

A complete sediment sequence was recovered from three holes; detailed records of magnetic susceptibility and density were generated to facilitate core correlation and to ensure that coverage was complete. The sediments of the one sedimentary unit cored are olive-green nannofossil clays with minor quartzose silt, volcanic ash, and clay. At the base (below 125 mbsf) we found layers enriched in organic carbon (about 1.5%) and distinctly laminated on a millimeter scale. The sequence at Site 963 spans the time interval from the early Pleistocene (1.5 Ma) to the Holocene. According to the preliminary shipboard assessment, the sediment section is complete and was deposited at rates between 85 m/m.y. in the section below 150 mbsf and up to 255 m/m.y. in the upper part of the section. The recovered sediments should therefore provide an excellent basis for the development of a high-resolution stratigraphy of the Pleistocene and the Holocene that are missing from the adjacent land sections in Sicily.

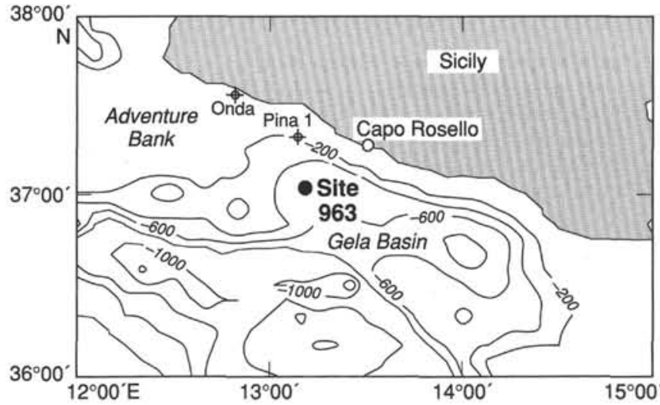

Figure 1. Location map of Site 963 in the Strait of Sicily, commercial wells (Pina 1 and Onda), and exposures on land (Capo Rosello). Bathymetry is from the ETOPO5 data set.

BACKGROUND AND OBJECTIVES

Site 963 is the westernmost location drilled during Leg 160 (Fig. 1). The location was chosen to recover and investigate sediments that record water exchange across and bottom-water characteristics of the Strait of Sicily. This shallow sill (the water depth of the two major channels of the strait is between 365 and 430 m) separates the western from the eastern Mediterranean sub-basin.

The ideal requirements for such a watchdog site at the exit of the Eastern Mediterranean are both stratigraphic continuity and high stratigraphic resolution. However, these requirements were difficult to meet in the region, where a combination of extensional and compressional tectonism created a complex and active relief in the Pleistocene (see "Geological Setting" section, this chapter). The drill location was chosen on the basis of extensive commercial multichannel seismic surveys near the southern margin of Sicily. It is situated on a low ridge on the gentle slope southeast of Adventure Bank in water 450 m deep. The low ridge separates a foredeep basin (Gela Basin) with thick Pliocene and Pleistocene deposits from a series of small intrashelf basins that are aligned roughly parallel to the southern coast of Sicily. At the site, seismic reflectors, interpreted as Pliocene-Quaternary sediments, are approximately 200 to 300 m thick and overlie an acoustic basement of unknown age (Fig. 2). Gravity cores taken at the location of Site 963 during a site survey recovered muddy sediments that were continuously sedimented at rates of 20 cm/k.y. for the last 50 k.y. (G. de Lange, pers. comm., 1995).

The primary scientific objective at Site 963 was to clarify paleoceanographic conditions on the sill that divides the two Mediterranean sub-basins. Under present-day conditions, Atlantic water is transported into the eastern Mediterranean basin by way of the North African Current, which flows along the African coast and passes through the Strait of Sicily. On its way to the Levantine Basin, evaporation is sufficiently high to increase surface salinities to an extent that convection of the surface water to greater depth occurs (see Fig. 3). The Levantine Intermediate Water is formed in this manner and then flows westward as part of the Mediterranean Intermediate Water at a depth interval between 200 and 600 m. MIW spills across the Strait of Sicily into the western Mediterranean and then through the Strait of Gibraltar into the Gulf of Cadiz and the North Atlantic. The present-day rate of MIW flowing westward across the sill is on the order of 700,000 m^3/s (Sarmiento et al., 1988). The water mass has oxygen concentrations averaging 190 µmol/L and exports nutrients from the eastern Mediterranean basin at a rate of 7×10^9 mol PO_4^{3-} per year (Fig. 3; after Béthoux, 1989; for different estimates, see Sarmiento et al., 1988).

The seafloor at Site 963 in the Strait of Sicily is in the water depth interval occupied by MIW. The variations in sedimentation and in the benthic record thus can be expected to reflect the variability in the formation of intermediate water and its properties.

A second important objective at the site was to correlate the submarine sedimentary record to well-studied land sections of marine sediments of Pliocene to middle Pleistocene age that are exposed in southern Sicily and in Calabria. Specifically, we aimed to bridge the stratigraphic gap between the youngest (i.e., early Pleistocene) sapropels exposed on land and the sapropel occurrences known from upper Pleistocene marine sediments of the eastern Mediterranean Sea. The land sections of Capo Rosello span the entire Pliocene; our objective was to expand that record to the Holocene.

GEOLOGICAL SETTING

Regional Tectonic and Depositional Setting of Site 963

The Strait of Sicily is located in an area affected by the convergence of Africa and Eurasia (see "Tectonic Introduction" chapter, this volume). Offshore southern Sicily lies on continental crust of the North African plate near the leading edge of the overriding crustal plate. In this area a promontory of Gondwana, represented by the Hyblean Platform, is in the process of irregular collision, giving rise to a complex tectonic scenario involving mainly northeast-oriented thrust faults in the overriding plate and mainly transtensional lineaments in the foreland (e.g., Malta, Linosa, and Pantelleria grabens).

Much information is available for the area surrounding Site 963 (e.g., Catalano et al., 1993a, 1993b; Di Stefano et al., 1993), notably concerning the Gela Nappe to the northeast and southeast and Adventure Bank to the northwest (Fig. 4). An interpretation of combined multichannel seismic data and well data suggests that major thrusting on the Gela Nappe last took place about 1.4 m.y. ago, followed by infill of the Gela Basin (Catalano et al., 1993a; Di Stefano et al., 1993). There is also evidence of large-scale submarine sliding on the inner shelf area, probably related to deformation of the Gela Nappe (Argnani, 1989; Trincardi and Argnani, 1990).

The foreland was drilled in the Onda well, to the northwest of Site 963 (Fig. 4). This comprises a 500-m succession of Pleistocene sediments (dated only from 115 m above the base), underlain by a stratigraphic gap extending to within the upper Pliocene, then 155 m of uppermost lower Pliocene and upper Pliocene sediments (Di Stefano et al., 1993). On multichannel seismic Line C529, the uppermost, horizontal reflectors are underlain by prominent, gently northward-dipping reflectors that may correspond to a paleontologically determined erosional hiatus (i.e., upper Pliocene–lower Pleistocene). The underlying, gently northward-dipping reflectors may thus correspond to a cored, mainly upper Pliocene interval (Di Stefano et al., 1993). These reflectors truncate underlying folded reflectors, possibly marking a second hiatus that was recognized near the top of the lower Pliocene interval.

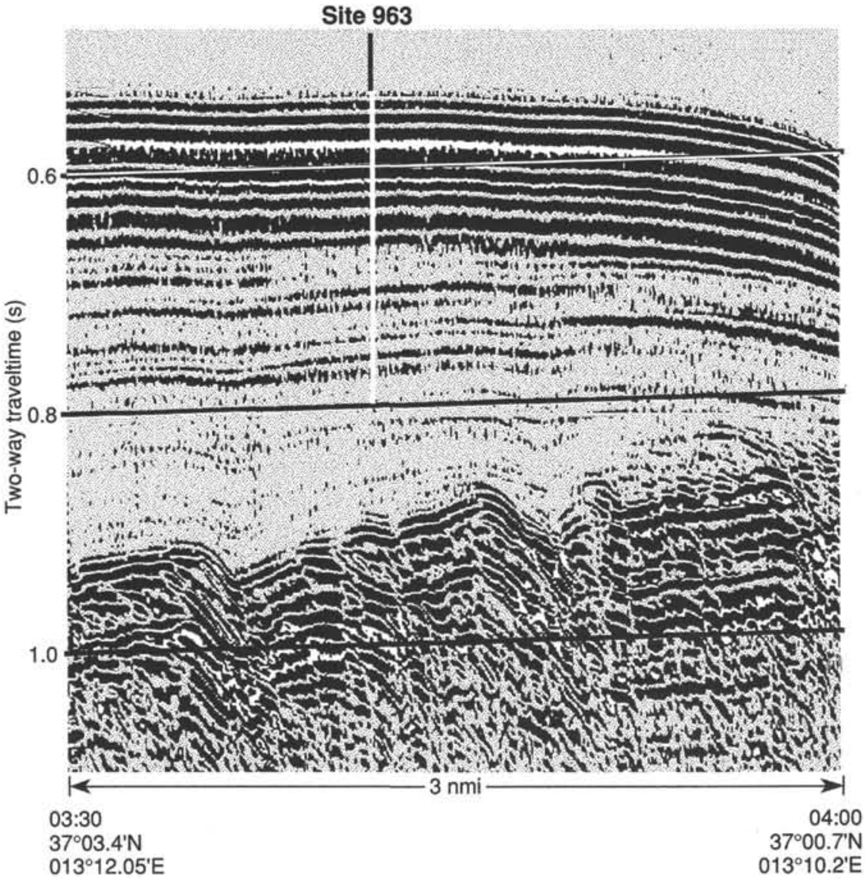

Figure 2. Portion of seismic line (single-channel air-gun Line SC2, *Tyro,* March 1993) showing the location of Site 963 and the approximate depth of penetration.

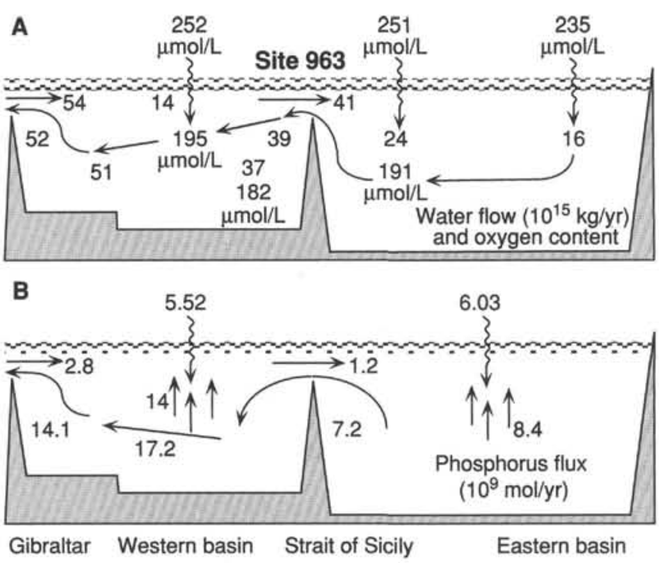

Figure 3. Schematic drawings of water exchange and oxygen content (**A**), and phosphorus flux (**B**). All values represent the present-day Mediterranean. After Béthoux (1989).

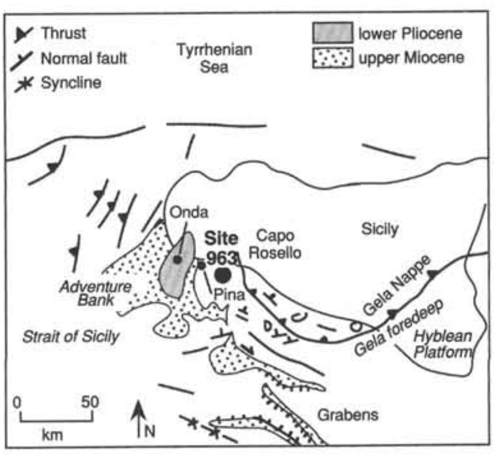

Figure 4. Tectonic interpretation of the Sicily offshore area, based mainly on industry seismic and well data. Simplified after Catalano et al. (1993b).

The reflecting horizons cored in the Onda well can be traced seismically to the Pina well, within the Gela Basin, farther southeast (Fig. 4). The Pina well recovered comparable, but expanded, successions to those cored in the Onda well, except that an additional 240 m of upper Pliocene–lower Pleistocene sediment was cored (Di Stefano et al., 1993). The probable cause of this difference is that crustal loading caused a pulse of flexural subsidence of the Gela Basin, and thus created additional space. On the foreland, a prominent acoustic surface above a tilted and deformed unit dated at 1.4 Ma can be traced beneath the leading edge of the Gela Nappe (Catalano et al., 1993a). This surface also shows some evidence of deformation. Overlying reflectors, of inferred early mid-Pleistocene age, can be traced into the Gela Basin, implying that major motion of the Gela Nappe did not take place until after the early Pleistocene. However, northward tilting has clearly taken place in inferred mid-Pleistocene time, giving rise to a sedimentary hiatus. The probable cause of this tilting is flexural loading, possibly related to thickening of the thrust wedge of the Gela Nappe in the hinterland.

Local Setting of Site 963

Site 963 lies in the foreland region, southeast of the Gela Basin on a relatively flat area on the southeastern slopes of Adventure Bank (Fig. 4). It lies within an embayment off the Linosa graben. The site-survey data (e.g., *Tyro* single-channel [SC] lines) for this area indicate an upper interval of nearly level reflectors (largely obscured by bubble pulses). Our own site-survey data reveal several minor low-angle discordances within the upper-level sedimentary succession drilled (see "Site Geophysics" section, this chapter), above a highly irregular, disrupted underlying reflector, of unknown age, but which may correlate with a similar disrupted reflector (of pre-early Pleistocene age) seen in industry Line C529 (Di Stefano et al., 1993).

The flat area of Site 963 is bordered by a series of basins bounded by inferred high-angle normal faults (Fig. 5). In several of these basins (e.g., north of Site 963) the lower, relatively transparent interval expands greatly into the basin, implying active subsidence during deposition. The upper reflective interval is draped over this basin, implying a relatively passive infill or one with only minor disturbance. By contrast, south of Site 963, the correlative upper reflective unit is downdropped into the more southerly of these two basins, implying the existence of young (?active) extensional faulting. The more southerly of these extensional faults was, in addition, imaged by our site survey (see "Site Geophysics" section, this chapter).

In summary, interpretation of Site 963 prior to drilling indicates that the site is located on a tectonically active foreland of the convergence zone between Africa and Eurasia, marked locally by the Gela Nappe system. Normal faulting of this area has been active throughout the Pliocene-Quaternary. The middle to late Pleistocene age determined at Site 963 is consistent with correlation with available seismic and well data. At Site 963 the underlying deformed and tilted reflectors represent the last major phase of thrusting of the Gela Nappe in this area at pre-early Pleistocene time. This would have caused flexural subsidence on the foreland and thus provided the accommodation space necessary for the accumulation of a well-preserved, tectonically undisturbed record of middle to late Pleistocene age at Site 963.

OPERATIONS

Marseille to Site 963

The last line in Marseille cleared the dock at 1309 hr local time on 12 March 1995. The 535-nmi sea voyage to proposed Site MEDSAP-4A required 50.7 hr at an average speed of 11.1 kt. A force 8 storm slowed progress to 7 kt at times with winds to 38 kt, 12-ft seas, and 15-ft swells. After a 20-nmi survey in 3.0 hr at 6.6 kt, a Datasonics 354M beacon was deployed at proposed Site MEDSAP-4A at 2150 hr on 14 March.

Hole 963A (Proposed Site MEDSAP-4A)

Hole 963A was spudded at 0435 hr on 15 March. The precision depth recorder indicated a water depth of 481.4 m, and the first core indicated a water depth of 481.0 m below rig floor (mbrf) by drill-pipe measurement (DPM). APC Cores 160-963A-1H through 25H were taken from 0 to 199.4 mbsf (Table 1), with 199.4 m cored and 203.17 m recovered (101.9% recovery). Cores were oriented from Cores 160-963A-4H through 25H. To improve recovery for high-resolution studies, the APC coring system was pushed beyond 150 mbsf into stiffer formation than normal. There was no bleed-off after Core 160-963A-5H, and overpull was 20 to 50 klb after Core 160-963A-6H. A total of 12 liners imploded and one burst from the stiff clay. Advance by recovery was used from Core 160-963A-11H (90.0 mbsf). There was no indication of suck-in. The maximum gas recorded was 270 ppm methane at Core 160-963A-9H (71.0 mbsf). Torque (to 400 amps) and overpull (to 40 klb) increased when the bit and BHA balled-up with clay. Coring was terminated for a short time while the string was rotated at 120 rpm and the pump rate increased, which reduced the problem. The bit cleared the seafloor at 2154 hr on 15 March, ending Hole 963A.

Hole 963B

The ship was moved 10 m to the northwest, and Hole 963B was spudded at 2235 hr on 15 March. The first core indicated a water depth of 480.5 mbrf by DPM. APC Cores 160-963B-1H through 24H were taken from 0 to 204.5 mbsf (Table 1), with 204.5 m cored and 206.2 m recovered (100.8% recovery). The lithology was the same as in Hole 963A, and the bit and BHA again had to be cleaned to reduce torque (to 700 amps) and overpull (to 50 klb). Five core liners imploded at the top and two liners had to be pumped out. The bit cleared the seafloor at 1231 hr on 16 March, ending Hole 963B.

Hole 963C

The ship was moved 10 m to the northwest and Hole 963C was spudded at 1340 hr on 16 March. The first core indicated a water depth of 480.0 mbrf by DPM. APC Cores 160-963C-1H through 6H were taken from 480.0 to 537.0 mbrf (0 to 57.0 mbsf) with 57.0 m cored and 57.93 m recovered (101.6% recovery).

Hole 963D

The ship was moved 10 m to the northwest, and Hole 963D was spudded at 1705 hr on 16 March. A single mud-line core was taken, which indicated a water depth of 480.1 mbrf. Core 160-963D-1H was taken from 0 to 8.4 mbsf with 8.39 m recovered. The BHA was secured for transit at 2200 hr on 16 March, ending Hole 963D. The drill collars were caked with about 7 cm of clay, proving that they were balled up. The beacon was recalled and recovered.

SITE GEOPHYSICS

The survey at Site 963 indicated that the region around the site varied little in geology from the site itself. As a result, the site survey during Leg 160 did not need to be extensive. A simple pattern of two lines across the proposed site was made, with an east to west connecting line between the southwest to northeast line and the northwest to southeast line (Fig. 6). The two new seismic profiles follow existing site-survey lines, to which they are strongly similar. The site itself lies just northeast of an incised and partially filled valley defined along its northeast side by what appears to be a fault showing a vertical displacement of about 600 ms two-way traveltime (TWT) (Fig. 7).

At the site, the new lines showed a strong reflector at just over 300 ms TWT. In the upper section are several strong continuous reflections at about 110 and 200 ms TWT, and another possibly at about 260 ms TWT, that are discernible through the interfering repetitions of the source signature. The lower reflectors show increasing amounts of subsidence with depth and lie unconformably on a horizon with small-scale relief (maximum amplitude of about 40 ms TWT) represented by the strong reflector. Below this the section shows dense high-amplitude chaotic internal reflections except for a deeper reflector that lies below the strong reflector at depths varying from 100 to 300 ms TWT. Because of the shallow water depth (about 310 ms TWT) and strong reflectivity of the seafloor and the major reflector below the upper sedimentary unit, a number of good multiples of various types observable deeper in the section have used multiple paths in the upper sediments as well as in the water column. The nature of the strong reflector beneath the upper sedimentary unit is unknown because drilling it was not permitted.

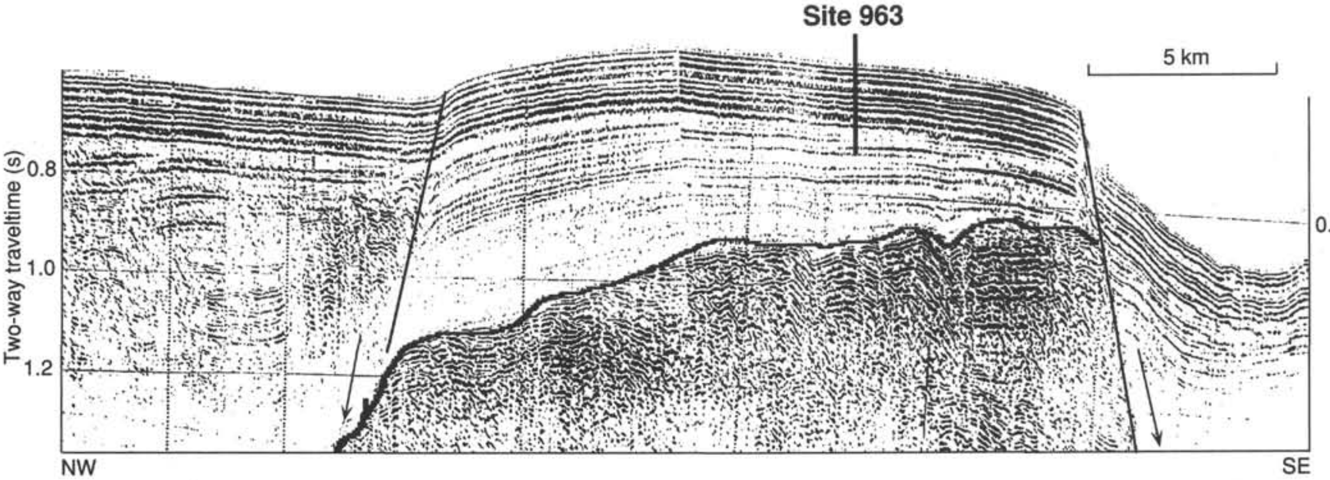

Figure 5. Setting of Site 963, based on *Tyro* single-channel seismic data (Line SC3). Note the extensional grabens on either side of the relatively flat, raised area drilled.

LITHOSTRATIGRAPHY

The 207-m sequence of early to late Pleistocene age sediment recovered from four holes at Site 963 consists of calcareous nannofossil clay with minor components of quartzose silt and volcanic glass. Several ash layers, up to 12 cm thick and commonly graded, occur within the upper 100 m. Below 125 mbsf, a series of darker colored layers, between 10 and 50 cm in thickness, occur. These are rich in pyrite and typically heavily bioturbated along their upper surfaces. The darkest of these layers, which occur near the base of the sequence recovered, are finely laminated. The only variation observed in the dominant nannofossil clay is a pale to dark color banding on a decimeter to meter scale.

The dominant lithology represented in the sequence at Site 963 shows no systematic downcore changes and consequently the sediments have been allocated to a single lithostratigraphic unit. Criteria employed in lithostratigraphic description and classification included (1) visual observation of color; (2) visual observation of sedimentary structures, including bioturbation; (3) smear-slide examination; (4) reflectance spectrophotometry measurements; (5) magnetic susceptibility and intensity measurements; (6) carbonate determinations; and (7) X-ray-diffraction (XRD) analysis.

Description of Lithostratigraphic Unit

Lithostratigraphic Unit I

Description: Nannofossil clay
Intervals: Cores 160-963A-1H through 25H, 160-963B-1H through 24H, 160-963C-1H through 6H, and 160-963D-1H
Depth: 0–199.4 mbsf, Hole 963A; 0–207.0 mbsf, Hole 963B; 0–57.0 mbsf, Hole 963C; 0–8.4 mbsf, Hole 963D
Age: late to early Pleistocene

The dominant lithology throughout is a nannofossil clay. The results of area-percentage determinations from smear-slide analyses indicate abundances of about 20%–40% nannofossils with the remainder comprising quartzose silt, volcanic glass, authigenic minerals (mainly pyrite), and minor amounts of foraminifers. No siliceous microfossils, other than rare sponge spicules, were recognized. Bulk-mineral analysis by XRD of unoriented powders shows a dominance of calcite and quartz with a component of clay minerals including kaolinite, chlorite, and illite. The results of calcium carbonate determinations (see "Organic Geochemistry" section, this chapter) indicate carbonate concentrations of between 20% and 45%.

Several cores within the upper 60 m of the section display little apparent color variation, although below 60 mbsf, there is some color variation within the dominant lithology, commonly from a paler light gray (10Y 6/1) to gray (10Y 4/1) or greenish gray (5GY 5/1).

Ash Layers

Thin layers of ash (tuffs) occur at fairly regular intervals in the upper 100 m of the section (Fig. 8). Six were found in Hole 963A and five in Hole 963B (Table 2), giving a total of seven (Fig. 9). The layers are up to 12 cm thick and exhibit normal grading with relatively sharp bases. The grains are generally angular to subrounded; the coarser fractions are up to 2 mm in diameter and consist of quartz, pumice, obsidian, and sporadic prismatic crystals of gypsum (or zeolite). The finer fractions are dominated by glass shards. All the ash layers are marked by peaks in the magnetic susceptibility records that can be correlated easily among Holes 963A through 963C.

Dark Gray Beds

Below about 120 mbsf, a series of darker gray (10Y 4/1 to 5Y 3/1) beds are present. They usually display a relatively sharp base and bioturbated top (see "Trace Fossils," below; Fig. 10). These beds contain significant amounts of pyrite compared to the background sediment and up to 1.49% organic carbon (Table 3; see "Organic Geochemistry" section, this chapter). Several beds contain abundant pyrite as framboids, microframboids, and small concretions, some of which are tabular. Foraminifers are also common. These beds become progressively darker and more organic rich with increasing depth, and at least two of the lowest examples (at Sections 160-963B-23H-2, 10–60 cm, and 24H-2, 40–110 cm) contain intervals with submillimeter, pale-dark laminae (Fig. 11).

The dark gray beds are picked out by several of the multiparameter measurements including total reflectance (L*), red/blue ratio (680 nm/420 nm), green reflectance (550 nm), magnetic susceptibility, and magnetic intensity (Fig. 12). The darkest colored layers are marked by an increase in magnetic intensity.

Trace Fossils

Discrete bioturbation structures were rarely observed in the upper 120 m. A vague mottling is present where color contrast and dark bluish black speckles (probably sulfides) mark the presence of scattered *Chondrites*-type burrows. Small pyrite concretions occur together with some pyritized burrows. Sporadic *Planolites* burrows were also

Table 1. Coring summary for Site 963.

Core	Date (March 1995)	Time (UTC)	Depth (mbsf)	Length cored (m)	Length recovered (m)	Recovery (%)
160-963A-						
1H	15	0340	0.0–4.5	4.5	4.52	100.0
2H	15	0405	4.5–14.0	9.5	9.81	103.0
3H	15	0425	14.0–23.5	9.5	10.00	105.2
4H	15	0455	23.5–33.0	9.5	9.86	104.0
5H	15	0525	33.0–42.5	9.5	9.98	105.0
6H	15	0555	42.5–52.0	9.5	9.84	103.0
7H	15	0630	52.0–61.5	9.5	9.21	96.9
8H	15	0655	61.5–71.0	9.5	9.58	101.0
9H	15	0730	71.0–80.5	9.5	9.95	105.0
10H	15	0800	80.5–90.0	9.5	10.03	105.6
11H	15	0910	90.0–98.6	8.6	8.63	100.0
12H	15	1000	98.6–108.1	9.5	9.95	105.0
13H	15	1035	108.1–115.1	7.0	7.00	100.0
14H	15	1110	115.1–124.6	9.5	9.71	102.0
15H	15	1145	124.6–133.6	9.0	8.04	89.3
16H	15	1230	133.6–143.1	9.5	9.75	102.0
17H	15	1315	143.1–151.5	8.4	8.51	101.0
18H	15	1340	151.5–156.5	5.0	5.29	106.0
19H	15	1425	156.5–162.5	6.0	6.03	100.0
20H	15	1505	162.5–170.5	8.0	7.96	99.5
21H	15	1550	170.5–176.5	6.0	6.20	103.0
22H	15	1635	176.5–186.0	9.5	9.87	104.0
23H	15	1720	186.0–192.0	6.0	6.00	100.0
24H	15	1805	192.0–197.5	5.5	5.47	99.4
25H	15	1900	197.5–199.4	1.9	1.88	98.9
Coring totals:				199.4	203.1	101.8
160-963B-						
1H	15	2140	0.0–9.0	9.0	8.97	99.6
2H	15	2200	9.0–18.5	9.5	9.85	103.0
3H	15	2220	18.5–28.0	9.5	9.75	102.0
4H	15	2250	28.0–37.5	9.5	8.08	85.0
5H	15	2345	37.5–47.0	9.5	9.86	104.0
6H	16	0005	47.0–56.5	9.5	8.53	89.8
7H	16	0040	56.5–66.0	9.5	7.75	81.6
8H	16	0135	66.0–73.0	7.0	6.34	90.6
9H	16	0230	75.5–82.5	7.0	9.70	102.0
10H	16	0255	82.5–92.0	9.5	9.28	97.7
11H	16	0340	92.0–100.7	8.7	8.84	101.0
12H	16	0415	100.7–108.9	8.2	8.21	100.0
13H	16	0435	108.9–116.9	8.0	8.10	101.0
14H	16	0500	116.9–126.4	9.5	9.48	99.8
15H	16	0530	126.4–135.9	9.5	9.89	104.0
16H	16	0555	135.9–142.4	6.5	6.51	100.0
17H	16	0625	142.4–148.9	6.5	6.54	100.0
18H	16	0650	148.9–158.4	9.5	10.07	106.0
19H	16	0720	158.4–165.4	7.0	6.91	98.7
20H	16	0805	165.4–174.9	9.5	9.91	104.0
21H	16	0840	174.9–183.4	8.5	9.69	114.0
22H	16	0915	183.4–189.9	6.5	6.64	102.0
23H	16	0940	189.9–197.5	7.6	7.60	100.0
24H	16	1005	197.5–207.0	9.5	9.69	102.0
Coring totals:				204.5	206.2	100.8
160-963C-						
1H	16	1245	0.0–9.5	9.5	9.49	99.9
2H	16	1315	9.5–19.0	9.5	9.94	104.0
3H	16	1340	19.0–28.5	9.5	9.96	105.0
4H	16	1405	28.5–38.0	9.5	9.78	103.0
5H	16	1425	38.0–47.5	9.5	9.91	104.0
6H	16	1455	47.5–57.0	9.5	8.85	93.1
Coring totals:				57.0	57.9	101.6
160-963D-						
1H	16	1610	0.0–8.4	8.4	8.39	99.9
Coring totals:				8.4	8.4	99.9

observed. Below 120 mbsf trace fossils were commonly observed within and around the darker gray beds described above. Commonly observed taxa include *Planolites, Zoophycos,* and abundant *Chondrites.* The dark gray laminated beds near the base of the hole generally display a relatively sharp base and onset of lamination in a bioturbation-free zone, but are extensively burrowed from the top in a tiered fashion with (downward) *Planolites, Zoophycos,* and *Chondrites* (Figs. 10, 13). *Zoophycos* burrows in stacks of up to seven spreiten are particularly common in, and immediately above, the darker beds. Long vertical burrows are sporadically present (e.g., Section 160-963B-11H-2, 65–90 cm; Fig. 14).

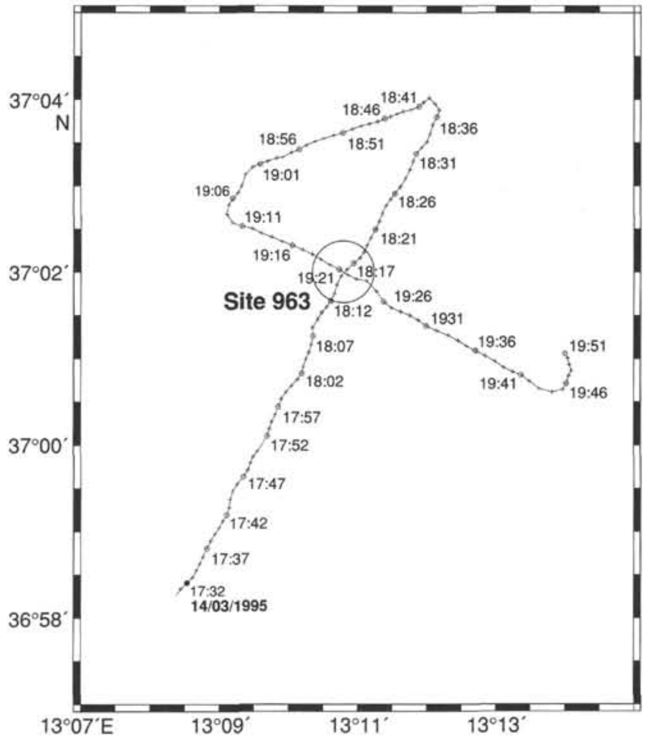

Figure 6. Track line of the survey across Site 963.

Paleoenvironmental Interpretation

The lack of sediment coarser than very fine silt and the absence of depositional sedimentary structures other than in the ash layers suggest sedimentation in a regime free of significant bottom currents, which is consistent with the site's relatively sheltered position. High sedimentation rates (>10 cm/k.y.) suggest an abundant supply of fine-grained material, together with rapid subsidence (see above). The abundance of reworked nannofossils suggests that some of the material present at Site 963 may have been eroded from older sequences, possibly by current scour in more exposed parts of the Strait of Sicily. Several ashes in the upper part of the sequence attest to regular volcanic activity in the late Pleistocene.

The dark gray beds in the lower part of the section indicate periods of enhanced deposition/preservation of organic matter. The abundance of pyrite indicates anoxic sulfidic diagenesis and the common *Zoophycos* burrows further suggest the presence of an enriched organic carbon food source (Kemp, 1995). The presence of these darker gray beds in the lower-middle Pleistocene of the sequence suggests that episodes of increased flux and/or preservation of organic matter occurred during this time. Fine lamination in some of these lower Pleistocene intervals confirms that local anoxic bottom-water conditions periodically excluded a burrowing benthos and preserved the sequential fluxes to the bottom sediment.

BIOSTRATIGRAPHY AND SEDIMENTATION RATES

Calcareous Nannofossils

The calcareous nannofossil biostratigraphy in Holes 963A, 963B, and 963C is typified by Pleistocene assemblages that commonly contain considerable quantities of reworked Pliocene, Miocene, Eocene, and Late Cretaceous species. Nannofossils are abundant in all of the slides analyzed. Preservation of the in situ Pleistocene specimens is

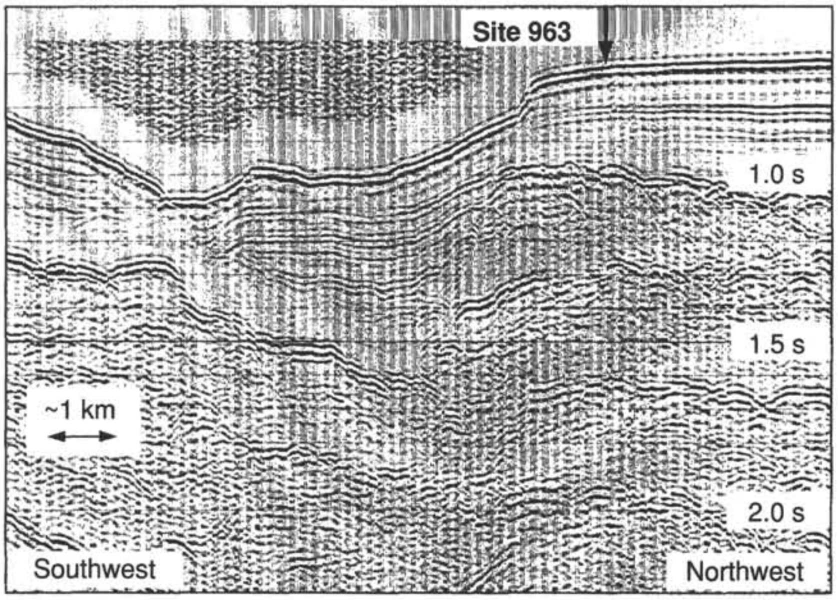

Figure 7. Seismic profile of Site 963.

good, whereas the reworked specimens observed exhibit moderate to good preservation. A summary of the biostratigraphic interpretations is reported in Figure 15.

Samples 160-963A-1H-CC through 3H-CC, 160-963B-1H-CC through 3H-CC, and 160-963C-1H-CC through 3H-CC contain nannofossils from Zone MNN21. This zone is identified by the presence of *Emiliania huxleyi.* The upper portion of this zone is usually subdivided based upon the acme of *E. huxleyi*; however, the acme could not be clearly distinguished during shipboard analysis. The accompanying assemblage includes small *Gephyrocapsa* (<3.5 µm), *Gephyrocapsa oceanica* s.l., *Helicosphaera kamptneri, Coccolithus pelagicus, Rhabdosphaera clavigera,* and *Pontosphaera japonica.* Specimens of *Discoaster barbadiensis, Discoaster saipanensis, Reticulofenestra umbilica, Ericsonia formosa, Sphenolithus heteromorphus, Sphenolithus abies, Helicosphaera ampliaperta, Pseudoemiliania lacunosa, Micula decussata,* and *Eiffellithus turriseiffelii* occur in varying quantities and indicate Pliocene, Miocene, Eocene, and Upper Cretaceous sources of reworking.

Samples 160-963A-4H-CC and 5H-CC, 160-963B-4H-CC, and 160-963C-4H-CC and 5H-CC are placed into Zone MNN20, which is a gap zone defined by the absence of both *E. huxleyi* and *P. lacunosa.* The shipboard placement of the upper boundary of this zone is tentative because *E. huxleyi* is typically rare near its first occurrence and difficult to recognize using a light microscope. The accompanying assemblage is similar to that found uphole. Reworking is similar in both quantity and assemblage to the preceding samples.

Samples 160-963A-6H-CC through 18H-CC, 160-963B-5H-CC through 19H-CC, and 160-963C-6H-CC contain nannofossils from Zone MNN19f. The upper boundary of the zone is defined by the first occurrence of *P. lacunosa,* whereas the lower boundary is defined by the first occurrence of *Gephyrocapsa* sp. 3. The placement of the upper boundary of this zone is difficult because *P. lacunosa* was found in rare abundances in samples uphole. The interpretation of where the zone begins in these samples is subjective and based solely upon an increase in abundance of *P. lacunosa* from rare to few. The uphole occurrences are interpreted as reworked, whereas the samples herein are considered in situ. The in situ and reworked assemblages that accompany *P. lacunosa* are similar to those found uphole.

Samples 160-963A-19H-CC through 21H-CC and 160-963B-20H-CC and 21H-CC contain nannofossils from Zone MNN19e. This interval is interpreted as a gap zone defined by the absence of both *Gephyrocapsa* sp. 3 and large *Gephyrocapsa* (>5.5 µm). Because *Helicosphaera sellii* was commonly found reworked upsection, the presence of large *Gephyrocapsa* (>5.5 µm) was used as a marker for the base of this zone. The accompanying in situ and reworked assemblages are similar to those found uphole.

Samples 160-963A-22H-CC through 25H-CC and 160-963B-22H-CC and 23H-CC contain nannofossils from Zone MNN19d. This zone is identified by the presence of both large *Gephyrocapsa* (>5.5 µm) and *H. sellii.* The accompanying in situ and reworked assemblages are similar to those found uphole.

Sample 160-963B-24H-CC contains nannofossils from Zone MNN19c. This zone is identified by the presence of *H. sellii* and the absence of both large *Gephyrocapsa* (>5.5 µm) and *Calcidiscus macintyrei.* The accompanying in situ and reworked assemblages are similar to those found uphole.

Planktonic Foraminifers and *Hyalinea baltica*

Planktonic foraminifers are generally common to abundant at Site 963 and consist of well-diversified and moderately to well-preserved Pleistocene faunas. However, the zonal boundary between the *Truncorotalia truncatulinoides excelsa* and *Globigerina cariacoensis* Zones was not recognized owing to the scarcity of *T. truncatulinoides excelsa.* In the Mediterranean, this species occurs discontinuously and its occurrence is strongly influenced by environmental factors (Di Stefano and Sprovieri, 1990; Fig. 15). At Site 963 it occurs only in Samples 160-963A-12H-CC and 13H-CC and 160-963B-11H-CC and 12H-CC.

Planktonic foraminiferal assemblages are relatively uniform throughout the sequence. They usually contain *Orbulina universa, Globorotalia inflata, Globigerinoides ruber, Globorotalia scitula, Globigerina bulloides, Turborotalita quinqueloba, Globigerinita glutinata, Globigerinita juvenilis,* and *Neogloboquadrina pachyderma* (both dextral and sinistral forms). Rare taxa include *Globigerinoides sacculifer, Pulleniatina obliquiloculata, Globigerinoides gomitulus, Globigerinoides pyramidalis, Globigerinoides conglobatus.*

Reworking has not affected the planktonic foraminiferal assemblages to the same degree as the nannofossil assemblages, although a few samples contain clearly reworked Miocene-Pliocene specimens (e.g., *Globigerinoides extremus, Paragloborotalia siakensis,* and *Turborotalita multiloba*).

An important Mediterranean Pleistocene marker is the benthic foraminifer *Hyalinea baltica.* It occurs in Pleistocene sediments and marks the base of the Emilian stage in the lower Pleistocene (Ruggeri

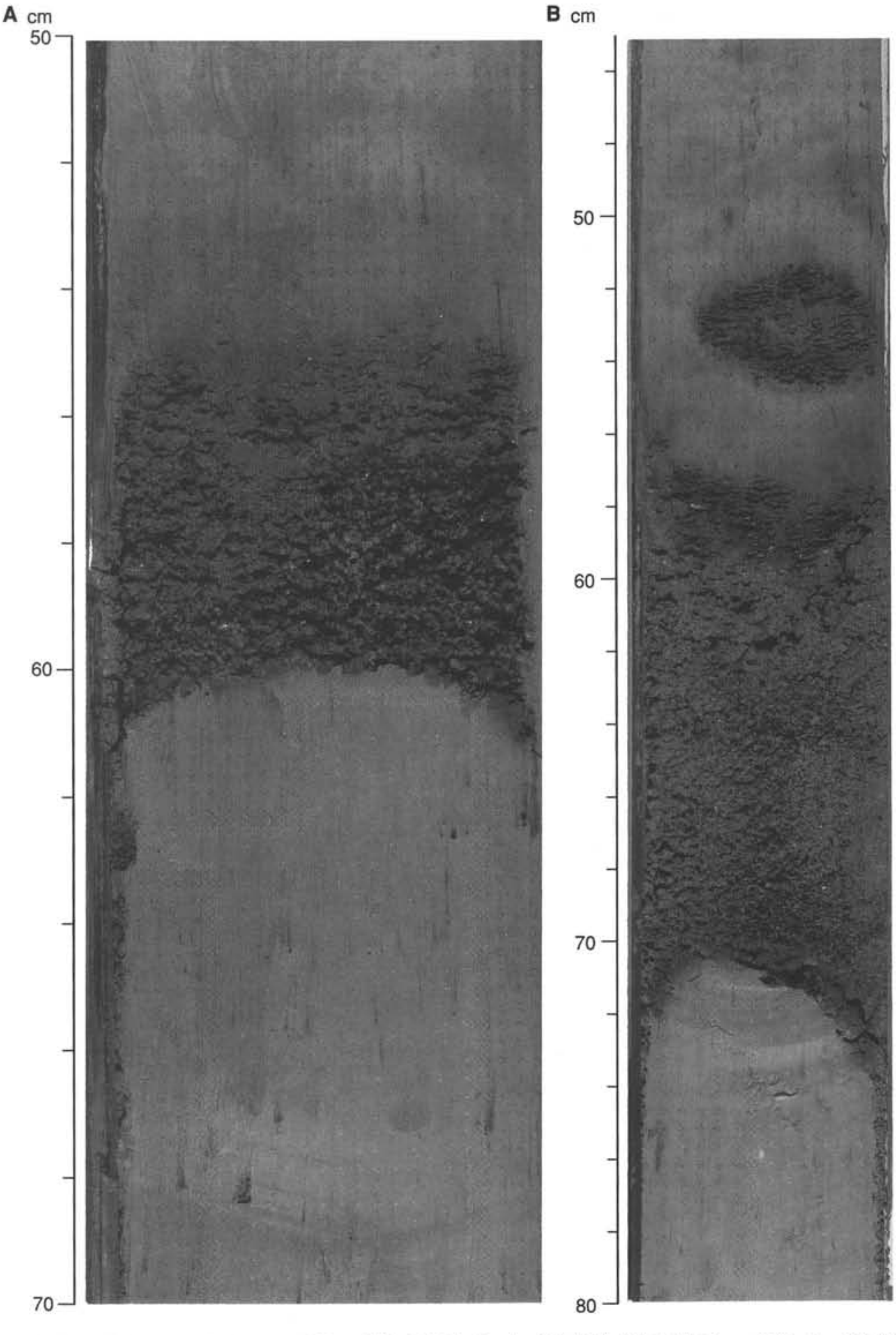

Figure 8. Coarse layers of volcanic ash present in the upper 100 m of Site 963 (**A.** Section 160-963A-3H-5, 50–70 cm; **B.** Section 160-963A-6H-3, 45–80 cm).

and Sprovieri, 1977). At Site 963 this form is present from Sample 160-963A-25H-CC upward (Fig. 15). However, its sporadic distribution at Site 963 most likely reflects changes in prevailing environmental conditions.

Sedimentation Rates

Sedimentation rates for Site 963 were estimated using calcareous nannofossil events and paleomagnetic reversal data detected in Holes 963A, 963B, and 963C (Table 4). The data are plotted on the age vs. depth curve shown in Figure 16. Error bars indicate the degree of uncertainty as to the location of the nannofossil events within a particular core.

Four significant shifts in sedimentation rates were determined from the Site 963 data. From the seafloor to the first occurrence of *E. huxleyi* (0.26 Ma) the sedimentation rate was approximately 111 m/m.y. Sedimentation rates increased to 195 m/m.y. in the interval from first occurrence of *E. huxleyi* to the last occurrence of *P. lacunosa.* Sedimentation

Table 2. Position of ash layers in Holes 963A and 963B.

Ash number	Depth (mbsf)	Location (core, section, interval in cm)
		160-963A-
1	20.55	3H-5, 50–60
2	46.20	6H-3, 50–70
3	62.30	8H-1, 86–96
4	65.05	8H-3, 55–57
5	78.80	9H-6, 30–42
6	100.50	12H-1, 97–100
		160-963B-
1	22.20	3H-3, 20–40
2	28.20	3H-7, 20–40
3	47.10	6H-1, 10–22
4	62.70	7H-6, 14–20
5	81.90	9H-5, 40–47

peaked at 255 m/m.y. in the interval from *P. lacunosa* to the bottom of magnetic reversal C1n. The sedimentation rates again declined to an average of 85 m/m.y. in the sediments recovered from the bottom of C1n to first occurrence of large *Gephyrocapsa,* an event that was observed only in Hole 963B.

PALEOMAGNETISM

Paleomagnetic measurements at Site 963 followed the methods discussed in the "Explanatory Notes" chapter (this volume). The natural remanent magnetization was routinely measured at 10-cm intervals on the archive half of each core section after AF demagnetization at 20 mT for Hole 963A and at 25 mT for Hole 963B. Rapid core recovery precluded demagnetization at more than a single level. NRM intensities were measurable throughout the 200-m stratigraphic interval recovered and were well above the noise level of the magnetometer (Fig. 17). Both the NRM intensity and the low-field magnetic susceptibility increase in magnitude with depth (Fig. 17). This suggests that downcore dissolution of magnetic minerals owing to reductive diagenesis is not a dominant process at Site 963, despite the rapid sedimentation rates (see "Biostratigraphy and Sedimentation Rates" section, this chapter).

The whole-core log of demagnetized inclination for Holes 963A and 963B is shown in Figure 18. The two records display a first-order similarity, particularly in the lower part of the sequence. However, this similarity is limited in extent. Discrete samples were taken from each section of core in Hole 963A in order to test the reliability of the whole-core measurements. Stepwise demagnetization of discrete samples reveals characteristic remanence components that are directed toward the origin of vector component diagrams (Fig. 19). In the upper part of Hole 963A, secondary components of magnetization are generally removed by peak AFs of 20 mT (e.g., Fig. 19A). However, in places, particularly lower in the sequence within the Matuyama Chron, the characteristic component may not be isolated below 40 mT (e.g., Fig. 19B, D). In many of the demagnetization diagrams, two secondary overprints are evident (e.g., Fig. 19B–D). The first overprint is easily removed at low AFs and is marked by a sharp decrease in remanence between 0 and 10 mT. This component is most likely a low-field isothermal remanent magnetization imparted to the core as it was raised through the drill string. An analysis of the directions associated with this overprint indicates that it has normal polarity (i.e., it is in the same sense as the present geomagnetic field) and is vertically oriented (Fig. 20). This direction is axial to the drill string and is easily removed, suggesting that the sediments at Site 963 have not been extensively remagnetized by the drilling process, in contrast to the problem that has plagued recent legs of the Ocean Drilling Program. The second overprint is more resistant to AF demagnetization (e.g., Fig. 19B–D). The directions associated with this component are consistent with normal polarity overprinting during the Brunhes Chron. In general, this component is of variable hardness and is removed at peak AFs between 10 and 40 mT. The curved portions of the demagnetization diagrams indicate that this secondary magnetization affects grains with coercivities that overlap those that carry the characteristic remanence component.

The highest AF that can be applied with the in-line demagnetizing coils on the shipboard cryogenic magnetometer is about 30 mT; however, this field cannot be applied routinely because heavy use causes the coils to heat to levels that could compromise future performance. The variable degree of contamination by secondary magnetizations at Site 963 means that the whole-core paleomagnetic record shown in Figure 18 does not faithfully record an accurate magnetic polarity stratigraphy (see Roberts et al., this volume, for further discussion). Furthermore, with the present in-line coils, it is not possible to achieve the desired level of demagnetization needed to construct a reliable magnetostratigraphy at Site 963. Although we applied a higher AF of 25 mT to core sections from Hole 963B, it is evident that these results are of similar quality to those from Hole 963A (Fig. 18). Nevertheless, results from stepwise AF demagnetization of discrete samples indicate that it is possible to isolate reliable characteristic remanence directions that enable the development of a magnetic polarity stratigraphy. Preliminary discrete-sample results from Hole 963A are shown in Figure 21 and the depths to the polarity boundaries are given in Table 5. The preliminary magnetic stratigraphy indicates that the sediments from Site 963 extend into the Matuyama Chron, with the Jaramillo Subchron clearly present. This magnetic polarity zonation is consistent with the micropaleontological zonations determined for Site 963 (see "Biostratigraphy and Sedimentation Rates" section, this chapter). Several short intervals of reverse polarity appear in the whole-core results from the Brunhes Chron (Fig. 18). At present it is not possible to distinguish whether these anomalous zones represent geomagnetic excursions or areas of disturbed magnetization in the core (see Roberts et al., this volume, for further discussion). Further work on samples from these intervals is aimed at determining the cause of the anomalous paleomagnetic directions.

STRUCTURAL GEOLOGY

Exposed structural features in the cores at Site 963 are rare. This may suggest a period of relative tectonic stability, although the lithologic homogeneity may obscure some structural features in the cores. Planar changes in color and grain size that may represent sedimentary bedding are consistently horizontal to subhorizontal with rare moderate dips in both holes (Table 6). Other features such as faint laminations (yellow to dark gray; see Fig. 11, "Lithostratigraphy" section, this chapter), thin dark gray to black layers and patches thought to be the result of pyrite or sulfide enrichment, and volcanic ash layers are also generally oriented horizontally with respect to the core coordinates. Slight to moderate dips (40°–48°, see Table 6) of coarser grained layers (up to 20 cm thick) are interpreted to result from slumping. Sharp and scoured basal contacts and gradational upper boundaries (Fig. 8, "Lithostratigraphy" section, this chapter) also show variations in dip (Fig. 22A). However, most bedding features are horizontal to subhorizontal with respect to the core coordinates.

Sporadic normal microfaults were observed at deeper levels (below 176.5 mbsf in Core 160-963A-22H, and 82.5 mbsf in Core 160-963B-10H; cf., Table 6). Shallowly dipping features, such as horizontal burrows and sedimentary bedding (Fig. 23) show offsets ranging from a few millimeters up to 8 cm. Although the data set is small, the consistent steep, north-south strike (with respect to the core reference frame) of planar to curviplanar fault surfaces measured in the cores suggests that these features formed under conditions of similar stress orientation.

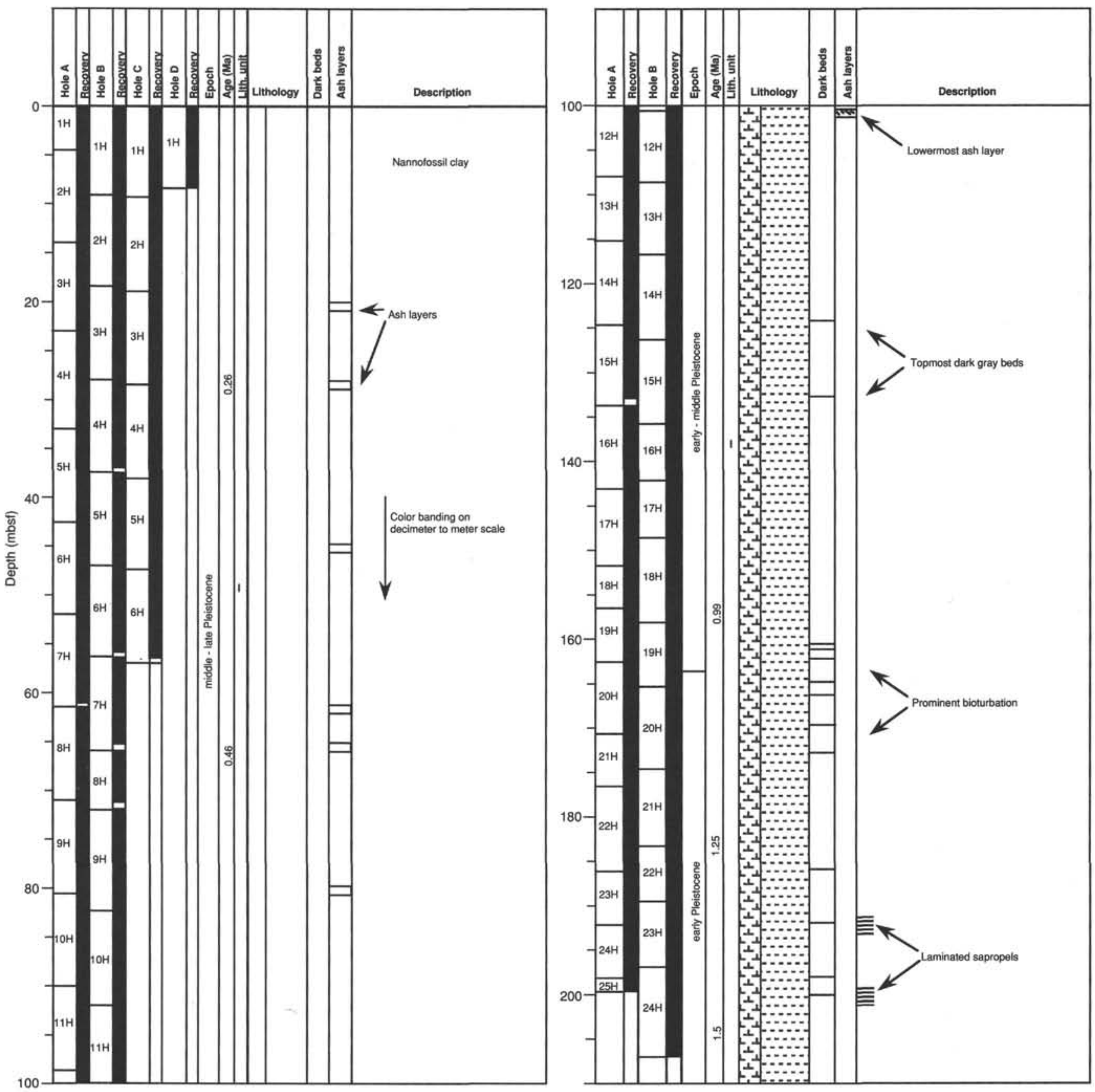

Figure 9. Core recovery, lithostratigraphy, and age for Site 963.

One possibility is that they were tectonically induced. The site is directly adjacent to a zone of extensional faulting and basin development (cf., Fig. 4, "Geological Setting" section, this chapter). There is also some evidence of possible faulting in the acoustic basement near the site (see "Site Geophysics" section, this chapter). It is possible that basement faults could have propagated up into the overlying sedimentary column, causing the high-angle normal faulting observed. Bearing in mind the existence of occasional minor slumping inferred from the inclined bedding surfaces, an alternative interpretation is that the faults record the effects of sediment compaction and soft-sediment deformation caused by sediment transport. Second, the drilling process possibly may have caused the formation of the microfaults owing to their consistency in orientation with respect to the core reference frame (see "Structural Geology" section, "Site 964" chapter, this volume). Normal faulting with minor offsets along steeply dipping planes is well known from deep-sea sediments obtained from other nontectonic settings (e.g., Ludden, Gradstein, et al., 1990).

Only two bedding planes and one fault plane measured in the core reference frame (Fig. 22) could be geographically corrected using orientation data from the Tensor tool (see "Explanatory Notes" chapter, this volume). Results are shown in Table 6.

COMPOSITE DEPTHS

High-resolution (2–10-cm scale) data collected on the MST and percent color reflectance from Holes 963A through 963D were used to determine depth offsets in the composite section. On the composite

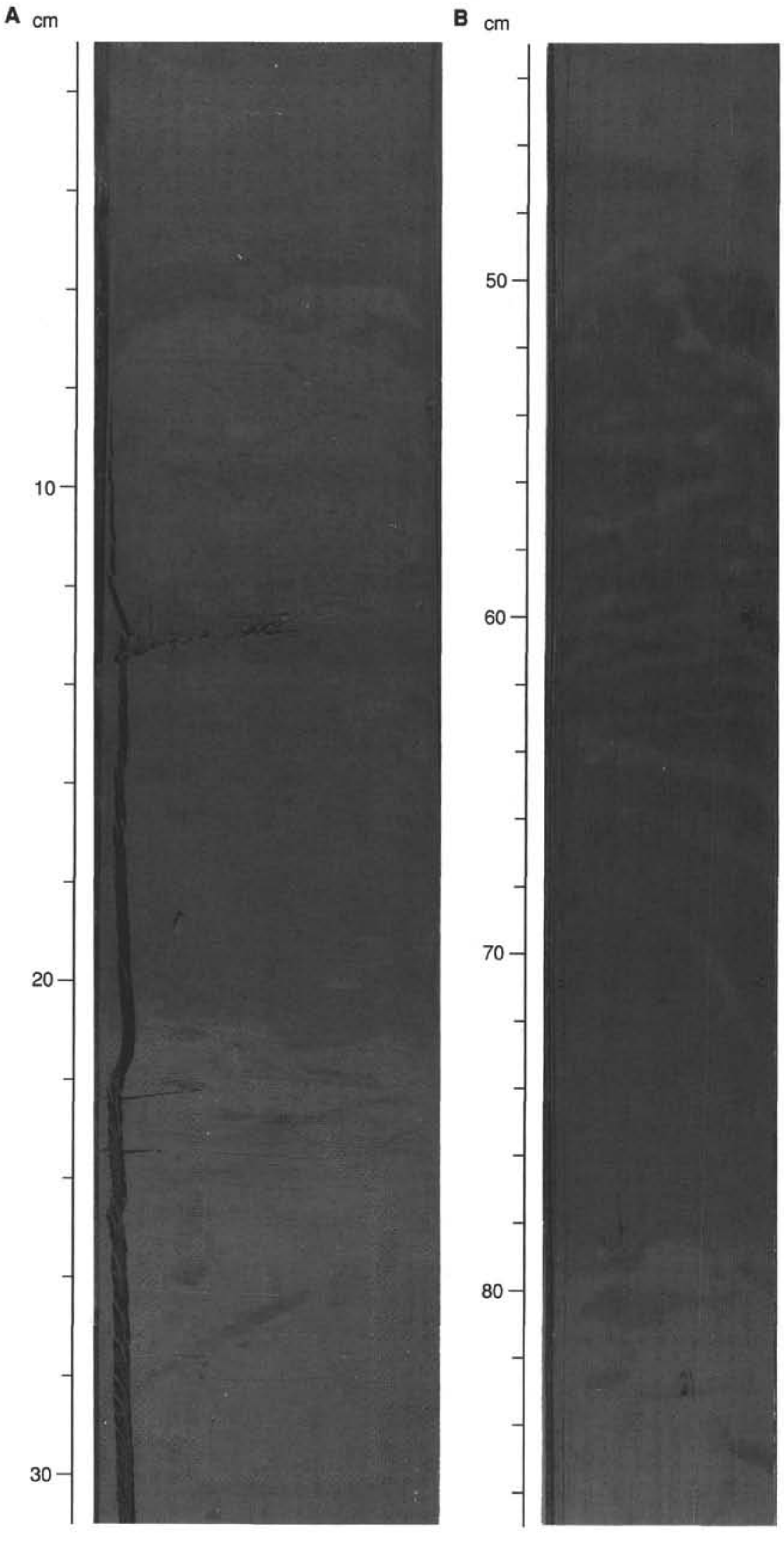

Figure 10. Dark gray beds in the lower to middle Pleistocene section (**A.** Section 160-963B-15H-5, 1–31 cm; **B.** Section 160-963A-20H-3, 43–87 cm). Note the intense bioturbation, mainly along the upper margin.

Table 3. Position of sapropels recovered at Holes 963A and 963B.

Number	Core, section, interval (cm)		Depth (mbsf)	Thickness (cm)	Laminated	TOC (%)
	160-963A-	160-963B-				
1		14H-5, 140–?	124.3	?40		1.49
2		15H-5, 5–21	132.6	16		—
3		19H-2, 20–50	160.4	20		1.03
4		19H-2, 60–85	160.75	25		0.85
5		19H-3, 60–85	162.25	25		1.05–1.15
6	20H-1, 97–132	19H-4, 75–110	165	35		0.92
7	20H-3, 50–79	20H-1, 74–103	166.43	29		1.13–1.24
8	20H-5, 45–115	20H-3, 66–137	169.77	70		1.15–1.44
9	21H-2, 25–80	20H-5, 140–?	172.8	55		1.04–1.22
10	23H-1, 15–65	22H-2, 30–100	185.9	?50–80		0.63–0.83
11		23H-2, 10–80	192.2	70	×	1.19–1.25
12	25H-1, 75–115	24H-1, 53–105	198	4050		0.68–0.83
13		24H-2, 55–105	200.2	250	×	1.16–1.23

depth scale, sedimentary features present in adjacent holes are aligned so that they occur at approximately the same depth. Working from the top of the sedimentary sequence, a constant was added to the depth in meters below seafloor for each core in each hole to arrive at a composite depth (mcd) for that core. The depth offsets that make up the composite depth section are given in Table 7. Continuity of the sedimentary sequence was documented only for the upper 110 mcd of the holes drilled at Site 963. Below 110 mcd, the continuity of the sequence could not be confirmed.

Magnetic susceptibility was the primary parameter used for correlation purposes at this site. GRAPE wet-bulk density variations were of low amplitude and thus not useful for composite depth construction. Natural gamma measurements were made throughout the entire section at all holes, but the sampling interval of 30 cm was insufficient for correlation purposes. Percent color reflectance measurements generally had a low signal to noise ratio but were of sufficient amplitude in a few intervals to provide additional support for composite construction.

The magnetic susceptibility records used to verify core overlap for Site 963 are shown on a composite depth scale in Figure 24. The cores from Holes 963A, 963B, and 963C provide continuous overlap to almost 110 mcd (base of Core 12H in Holes 963A and 963B). Cores 160-963A-8H and 9H and 160-963B-8H and 9H do not appear to overlap at 75 mcd. This lack of overlap is an artifact of MST processing. Sections 5 and 6 of Core 160-963A-8H (2.08 m of sediment) were not run through the MST. Correlation of percent reflectance data across this interval, however, confirms the overlap. Below 110 mcd, interhole offsets are lacking at several depth intervals (110–140 and 200 mcd). Across these intervals, successive cores were placed at original (mbsf) depths plus the accumulated mcd offset. It is not clear how much core, if any, is missing across these core breaks. Stratigraphic continuity also cannot be confirmed between Cores 160-963B-21H and 22H as the record in Hole 963A cannot be unambiguously tied to the Hole 963B cores over this interval.

Stretching and compression of the sedimentary features in aligned cores indicates distortion of the cored sequence. Because much of the distortion occurred within individual cores on depth scales of less than 9 m it was not possible to align every feature in the susceptibility records accurately by simply adding a constant to the mbsf core depth. Within-core scale changes will require post-cruise processing to align smaller sedimentary features.

Following construction of the composite depth section for Site 963, a single spliced record was assembled from the aligned cores. The Site 963 spliced record can be used as a sampling guide to recover a single sedimentary sequence. The spliced record consists primarily of cores from Holes 963A and 963B. One core from Hole 963C was used to construct the sampling splice. A small depth discrepancy may result when comparing depths generated from the offset depth table (Table 7) with a downcore record (e.g., magnetic susceptibility) generated using the splice table (Table 8). This discrepancy results

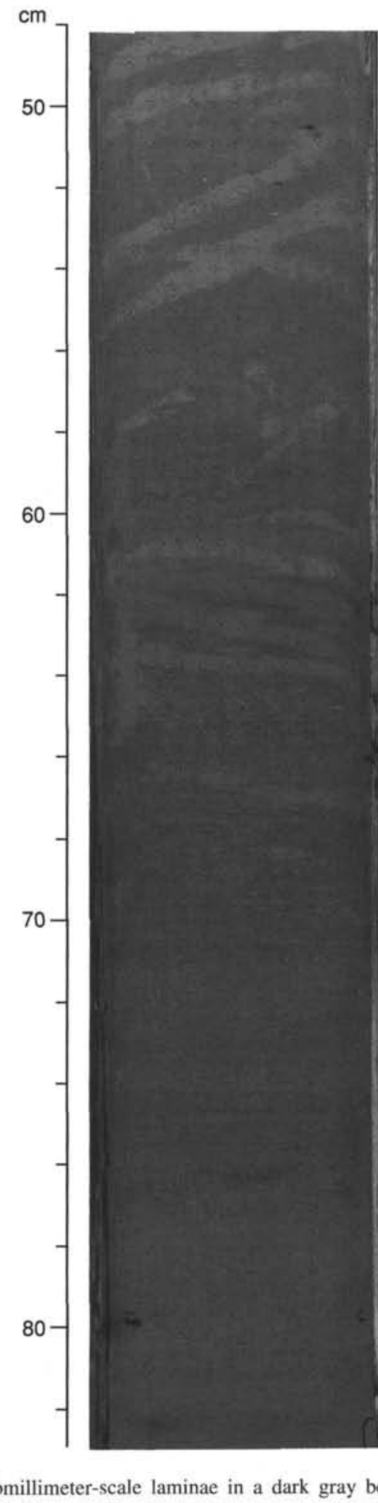

Figure 11. Submillimeter-scale laminae in a dark gray bed (Section 160-963B-24H-2, 48–83 cm). The paler sediment above the dark gray bed has been brought down and mixed in the upper part by *Zoophycos* and *Chondrites* burrows.

from slight misalignments of the stratigraphic features (see previous paragraph) used to make the splice. Intervals with significant disturbance or distortion were avoided if possible. As mentioned above, several intervals did not have unambiguous overlap among the holes. In each of these cases, cores from Hole 963A were appended to the splice. The tie points for the splice are given in Table 8.

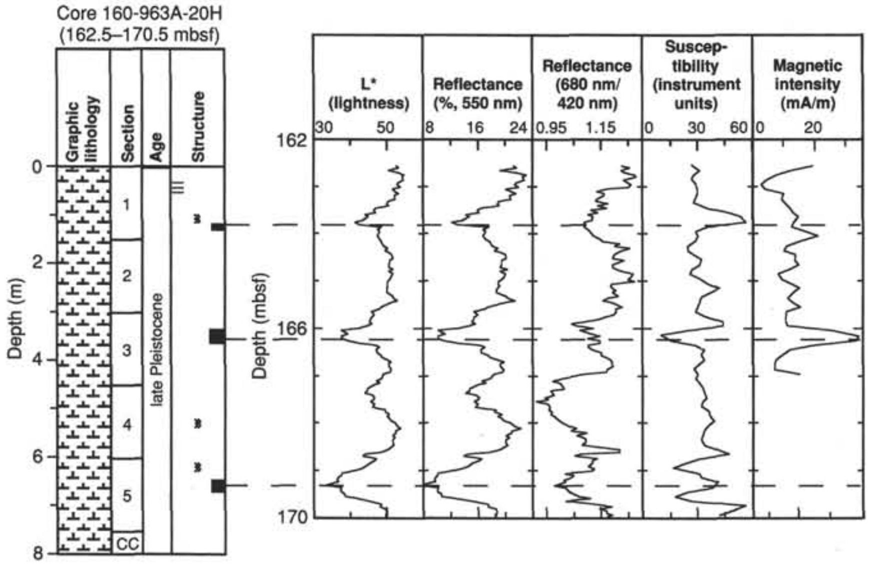

Figure 12. Plots of lithology and multiparameter data including color intensity, red/blue (680 nm/420 nm ratio), magnetic susceptibility, and magnetic intensity (after 20-mT demagnetization).

INORGANIC GEOCHEMISTRY

Interstitial-water samples were obtained at Site 963 from 1.45 to 194.90 mbsf, using both the standard ODP titanium/stainless-steel squeezer (Manheim and Sayles, 1974) and a Teflon-lined squeezer (Brumsack et al., 1992). In total, 12 samples were squeezed (Table 9). The retrieved pore waters were subsequently analyzed for salinity, alkalinity, chloride, sulfate, bromide, lithium, potassium, rubidium, sodium, calcium, magnesium, strontium, ammonium, and silica by the methods described in the "Explanatory Notes" chapter (this volume).

Salinity, Chlorinity, Potassium, Rubidium, and Silica

Salinity decreases from a typical Mediterranean bottom-water value of about 38 g/kg to a value that is 10% lower, at 140–150 mbsf (Fig. 25). This magnitude of change is not seen in the chloride profile, which decreases only by 3% (Fig. 25). The salinity decrease corresponds to the reduction in sulfate due to bacterial activity and the diagenetically induced calcium and magnesium depletions that are discussed below. A nearly 50% decrease in the potassium and rubidium concentrations is observed in the pore waters at Site 963 (Fig. 25). Similar decreases observed at many ODP sites are attributed to the uptake of potassium by clay minerals or the alteration of volcanic ash layers (Gieskes, 1981, 1983). The concentration of dissolved silica varies between 200 and 300 µM in a way that seems to be unrelated to other pore-water constituents. Usually, the concentration of silica is determined largely by equilibrium with minerals such as opal and clay minerals. On the basis of the concentrations observed at Hole 963A, no appreciable amounts of amorphous silica (opal, diatoms, radiolarians, etc.) seem to be present.

Organic Matter Degradation

Degradation of sedimentary organic matter affects the pore-water composition at Site 963 in two distinct intervals, from 0 to 10 mbsf and from 60 to 160 mbsf. On the basis of the ammonium and bromide profiles, this degradation seems to be most pronounced in the upper interval (Fig. 26). The sulfate vs. depth profile (Fig. 26) indicates sulfate-reducing conditions in the upper 40 m, without a distinct sulfide odor discerned. Evidently, the amount of reactive iron oxy/hydroxides is more than sufficient to trap all free sulfide. From 60 to 160 mbsf methane generation occurs (see "Organic Geochemistry" section, this chapter). In view of the upward methane flux, approximately one-third of the sulfate decrease must result from methane oxidation and, consequently, two-thirds is attributed to sulfate reduction. The rapid release of ammonium during the decomposition of organic matter in the top 10 m may induce ion exchange reactions at mineral surfaces with a corresponding uptake of some ammonium and release of lithium. This is seen in the abrupt increase in lithium in the top 10 m (Fig. 26). The increases in lithium and sulfate below 160 mbsf are discussed below.

Carbonate Diagenesis

In the pore-water profiles for calcium and magnesium, large decreases occur that are unrelated to changes in chlorinity (Figs. 25, 27). Major decreases in pore-water magnesium concentrations have been attributed to interaction with volcanic (ash) layers (Gieskes, 1983). In the upper 100 mbsf several distinct ash layers were observed (see "Lithostratigraphy" section, this chapter). However, the interaction with volcanic ash is not likely to cause the observed changes at this site, as there is no corresponding increase in calcium. As stated above, at Site 963, a corresponding decrease in both calcium and magnesium was observed. Moreover, the concave shape of both profiles suggests a continuous process of calcium and magnesium removal in an approximately 1:5 ratio.

The measured alkalinity is far less than that calculated from the observed ammonium concentration and an assumed Redfield C/N ratio of 6.6 for the organic matter. It must be noted here that this underestimates the real bicarbonate (alkalinity) production, because some ammonium is taken up at mineral surfaces (see above), and the C/N ratio of decomposing organic matter in Eastern Mediterranean sediments seems to be 20–30 rather than 6.6 (G. de Lange et al., unpubl. data).

The observed calcium, magnesium, and alkalinity decreases all point to the formation of a disseminated (high) magnesium-calcite phase in the sediments of the upper part of this site. The formation and occurrence of magnesium calcites in the Eastern Mediterranean is widespread (e.g., Emelyanov, 1972; Stanley, 1972; Milliman and Müller, 1973).

Assuming a sulfate-reduction/methane-oxidation ratio of 2 (see above), the difference between the calculated and observed alkalinity is 48 meq/L, which equals 24 mM of CO_3^{2-}. The total decrease in the magnesium plus calcium concentration equals 24 mM, which agrees with the proposed precipitation of a magnesium-calcite phase.

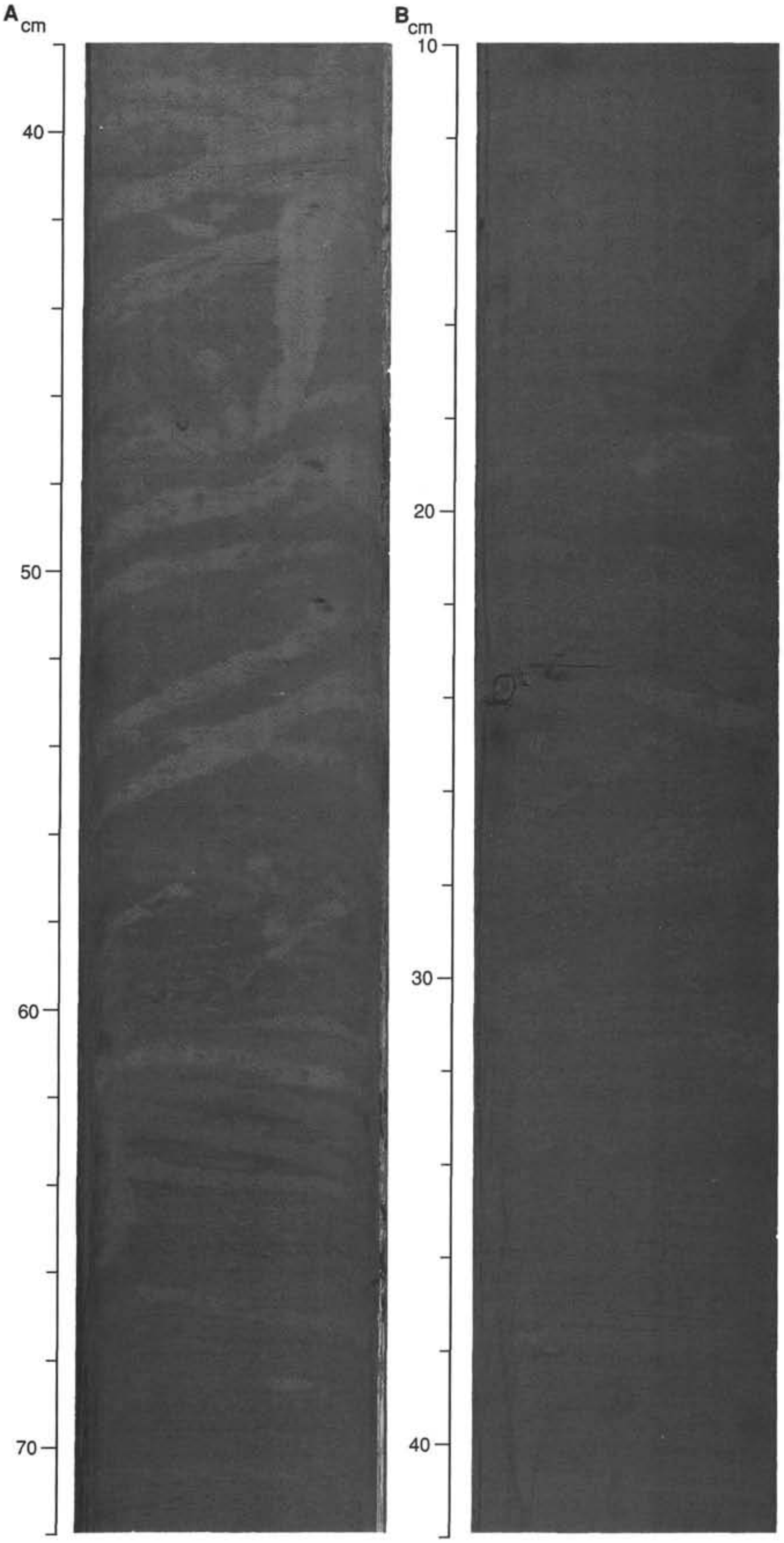

Figure 13. Trace fossils in and adjacent to a dark gray bed including *Planolites, Zoophycos* with well-developed spreiten, and locally intense *Chondrites* (**A.** Section 160-963B-24H-2, 38–72 cm; **B.** Section 160-963B-23H-2, 10–41 cm).

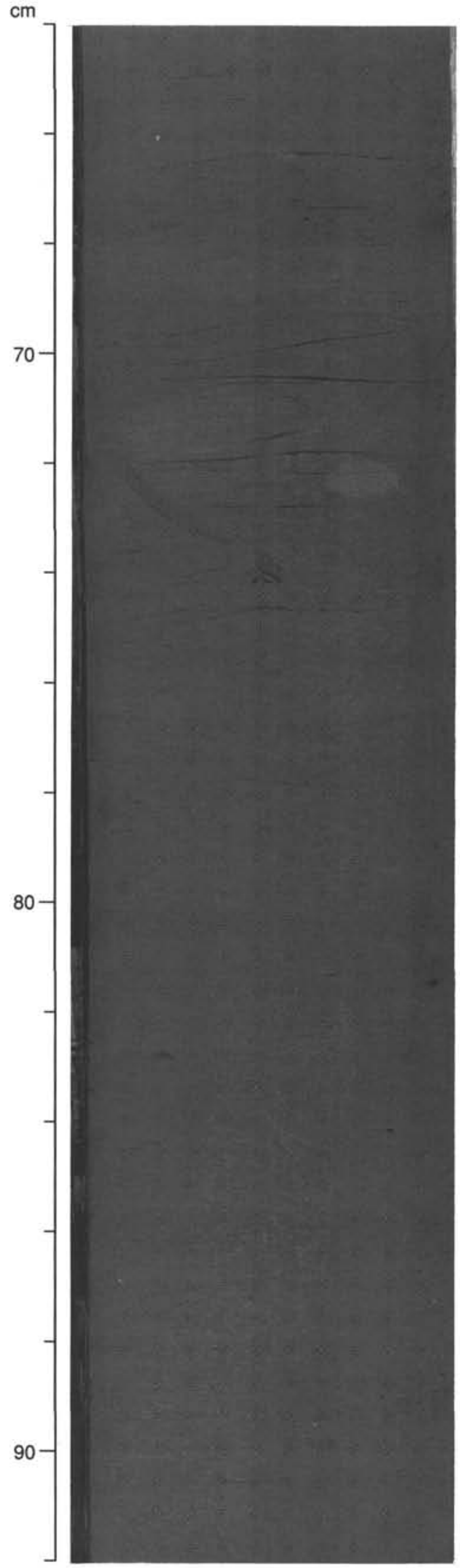

Figure 14. Unusual, long vertical burrow in lower to middle Pleistocene sediments. Note the *Chondrites* fill (Section 160-963B-11H-2, 64–92 cm).

We can also estimate the C/N ratio of decomposed organic matter, assuming no major uptake of ammonium by minerals. The calculated bicarbonate generated by sulfate reduction is 40 mM, and the associated ammonium increase is 1.8 mM. Consequently, the estimated C/N ratio of decomposing organic matter is approximately 22. It must be noted here that different diffusivities for bicarbonate and ammonium have not been taken into account in these rather rough estimates.

Evaporite-Related Fluxes

In the lower part of Site 963, a distinct increase is observed in the concentrations of sulfate, calcium, strontium, and lithium, with a calcium to sulfate ratio close to 1. Furthermore, several organic-rich intervals are present at the base of Hole 963A, and by extrapolation from Hole 963B, even more organic-rich intervals should be present just below the bottom of Hole 963A. Consequently, one would expect sulfate concentrations to decrease near the bottom of Hole 963A, owing to the anticipated sulfate reduction. In contrast, we observed an increase in sulfate.

The increase in chloride in the lower part of this site is within analytical error (1% or less). In addition, there is no significant increase in the concentration of bromide, potassium, magnesium, or sodium. Consequently, there is no geochemical indication for a late- or early-stage evaporite at depth. At this relatively shallow site, one would expect gypsum rather than halite or late-stage evaporites to underlie the post-Messinian sediments. This coincides with the observed increases of calcium, strontium, and sulfate concentrations vs. depth in the lower part of this site (Figs. 26, 27).

The significant increase of lithium from 110 to 200 mbsf does not seem to fit this picture, as the lithium content in gypsum usually is rather low. In contrast, its concentration in late-stage evaporites is considerably enhanced. At present we have no satisfactory explanation for the behavior of lithium at the base of this site.

ORGANIC GEOCHEMISTRY

Volatile Hydrocarbons

As part of the shipboard safety and pollution-prevention monitoring program, hydrocarbon gases were analyzed in each core of Hole 963A by the headspace technique. Only minor concentrations of methane in the range of 2 to 270 ppm were recorded. The results are reported in Table 10 and graphically displayed vs. depth in Figure 28. Methane concentrations were consistently low down to 60 mbsf. The significant rise below this depth coincides with sulfate depletion by microbial sulfate reduction (see "Inorganic Geochemistry" section, this chapter). The gradual decrease of methane concentrations from about 120 mbsf to the bottom of Hole 963A is probably caused by the reinstallation of microbial sulfate reduction owing to sulfate supply from below. Under these conditions, methane may be progressively depleted by methane-oxidizing bacteria.

Carbon, Nitrogen, and Sulfur

The abundances of total, inorganic, and organic carbon, calcium carbonate, total nitrogen, and sulfur in the sediments from Holes 963A and 963B are summarized in Table 11. Random sampling was performed for Hole 963A, with additional samples taken from the darker green intervals in the lower part of the hole. Samples from Hole 963B were selected to contrast light/dark alternations in Cores 160-963B-14H through 24H.

Carbonate contents do not deviate significantly from 20% in the upper 80 m of Hole 963A (Fig. 29). They appear to pass a maximum at about 145 mbsf with strong (cyclic?) fluctuations. Below 140 mbsf, much of the small-scale variation is due to the higher carbonate contents of the light-colored sediments compared to the dark-colored

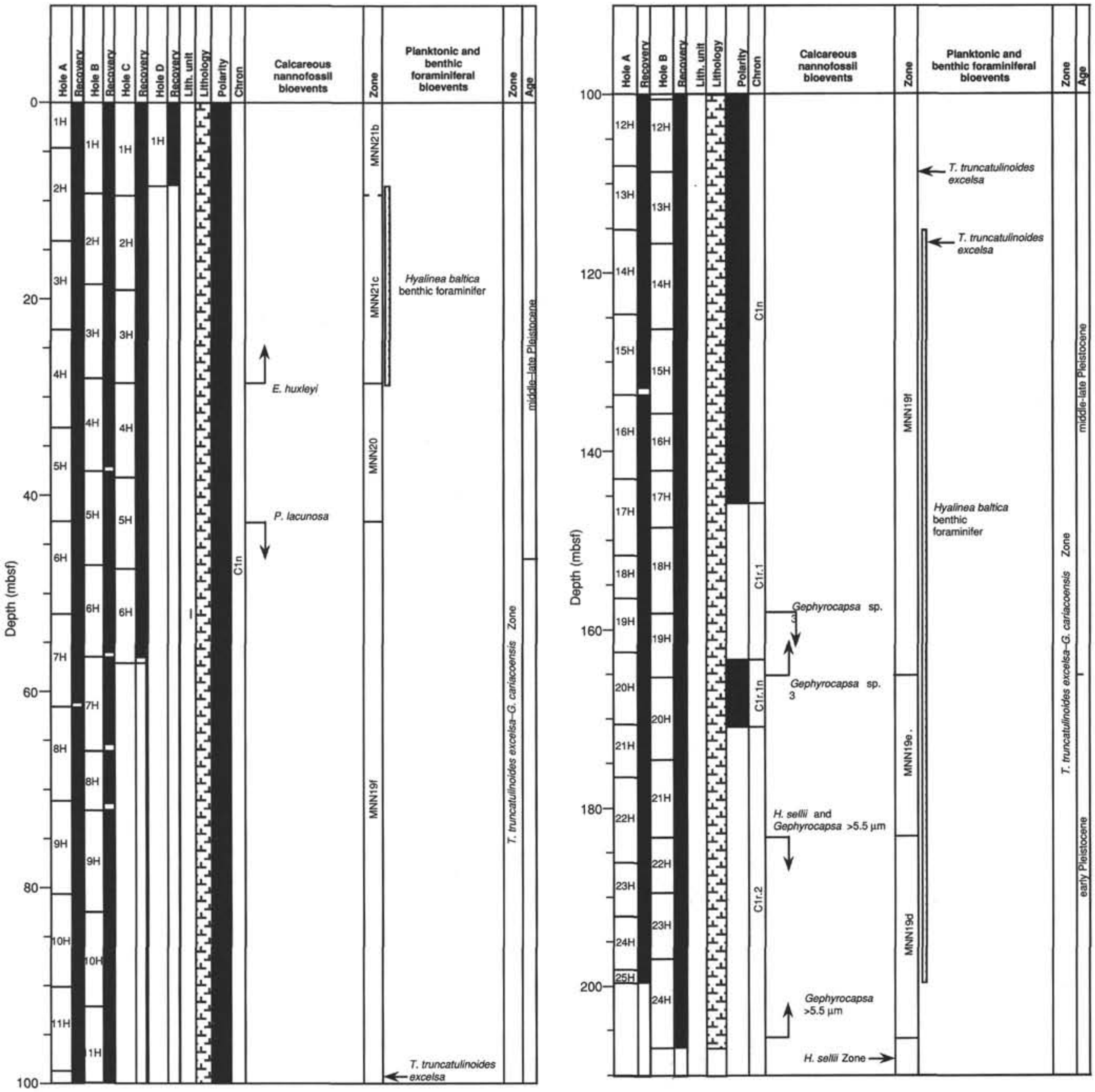

Figure 15. Composite of biostratigraphic events recognized at Site 963 in Holes 963A, 963B, and 963C including lithostratigraphic and magnetostratigraphic records. The dotted bar marks the distribution of the benthic foraminifer *Hyalinea baltica*. The base of the *Emiliania huxleyi* acme could not be identified with confidence during shipboard analysis.

sediments. This latter pattern also occurs in the lower part of Hole 963B (Fig. 30).

Organic carbon values in Holes 963A and 963B are consistently below 0.5% for the light-colored sediments, both in the upper part of the profile and in the sections with light/dark alternations (Table 11, Figs. 29, 30). In the dark-colored sediments, the organic carbon contents vary mostly between 0.7% and 1.5%.

The low C_{org}/N ratios (Table 11, Figs. 29, 30) for the organic-matter-lean sediments are certainly due to an inorganic nitrogen component in the N value, and, thus, the ratios are not meaningful in terms of organic matter source indicators. C_{org}/N ratios mostly of about 7 to 9 for those sediments containing more than 0.7% C_{org} may indicate a dominance of marine organic matter, but the general covariation with the organic carbon values suggests at least some contribution of inorganic nitrogen that leads to a possible underestimation of the terrigenous organic matter component. Sulfur values are reported in Table 11, but cannot be interpreted because further investigations are required to account for the pyrite and elemental sulfur fractions.

Rock-Eval Pyrolysis

Rock-Eval pyrolysis was performed for selected organic-carbon-rich samples from Holes 963A and 963B (Table 12). Hydrogen indices are low throughout, indicating that none of the sediments contains

Table 4. Stratigraphic list of calcareous nannofossil events and paleomagnetic reversals for Site 963.

Event	Hole, core, section, interval (cm)	Depth (mbsf)	Depth (mcd)	Age (Ma)
FO *E. huxleyi**	963C-3H-CC	28.5	28.71	0.26
	963A-4H-CC	33.00	36.09	
LO *P. lacunosa*	963B-7H-CC	64.25	67.64	0.46
	963C-6H-CC	52.34	55.99	
Bottom C1n	963A-17H-2, 82	145.52	149.23	0.78
Top C1r.1	963A-17H-3, 45	146.55	150.36	
Bottom C1r.1	963A-19H-4, 39	160.98	164.39	0.98
Top C1r.1n	963A-20H-2, 112	165.12	168.93	
FO *Gephyrocapsa* sp. 3	963A-19H-CC	156.79	160.60	0.99
	963B-19H-CC	158.97	166.31	
Bottom C1r.1n	963A-20H-4, 95	167.55	171.36	1.07
Top C1r.2	963A-21H-1, 88	171.38	175.19	
LO *Gephyrocapsa* >5.5 µm	963A-23H-CC	192.00	196.32	1.25
	963B-21H-CC	183.40	188.64	
FO *Gephyrocapsa* >5.5 µm	963B-24H-6, 81	205.81	210.24	1.50

Notes: FO = first occurrence; LO = last occurrence; * to be confirmed by scanning electron microscopy.

a significant amount of unaltered hydrogen-rich marine organic matter. Extensive microbial degradation of the labile organic matter fraction probably occurred during sulfate reduction and methanogenesis. In addition, oxidation of marine organic matter during settling through an oxygen-rich water column and a terrigenous organic matter component in the sediments may have contributed to the low hydrogen indices. Oxygen indices above 150 are consistent with this interpretation. However, care should be taken in interpreting oxygen index values for thermally immature and young sediments because labile carbonates may have decomposed below 390°C during pyrolysis and thus added CO_2 to that derived from organic matter.

PHYSICAL PROPERTIES

Physical properties were measured in all cores obtained at Site 963. Measurements were conducted on whole-round core sections using the MST, which comprises the GRAPE, *P*-wave velocity logger, natural gamma-ray device, and magnetic susceptibility meter. Thermal conductivity was measured in whole core sections (see "Explanatory Notes" chapter, this volume, for technical details of these procedures). In addition, a detailed suite of physical property measurements was performed on selected split core sections from Hole 963A; these measurements included dry- and wet-bulk density, grain density, porosity, water content, and void ratio. Vane shear strength and compressional wave velocities were measured in split core sections from Hole 963A.

Physical properties measured using the MST were obtained from all core sections from Holes 963A through 963D, with the exception of core catchers and some very short sections. Thermal conductivity, index properties, shear strength, and velocity measurements were taken for two sections of each core from Hole 963A. The physical properties measurements are listed in Tables 13 through 16, and are shown graphically in Figures 31 through 37. In this section, we describe the downhole distribution of selected physical properties of Hole 963A.

Index Properties

The measured index properties include measurements of the mass and volume of selected sediment samples, from which water content, bulk and dry density, bulk and dry porosity, void ratio, and grain density were calculated (Table 13).

Measured wet-bulk density generally increases with depth (Fig. 31), owing to compaction and diagenesis. Wet-bulk density values in the upper 30 m of the hole show an abrupt increase from 1.62 to 1.8 g/cm^3. Farther downhole, the increase in the wet-bulk density is moderate, and values of approximately 1.85 g/cm^3 were measured at a depth of almost 200 mbsf. Water content, expressed relative to dry weight, varies from almost 45% just below the seafloor to approximately 30% at a depth of 50 mbsf (Fig. 31). From that depth downward, changes in water content with depth are moderate, and values of 25% were measured at almost 200 mbsf.

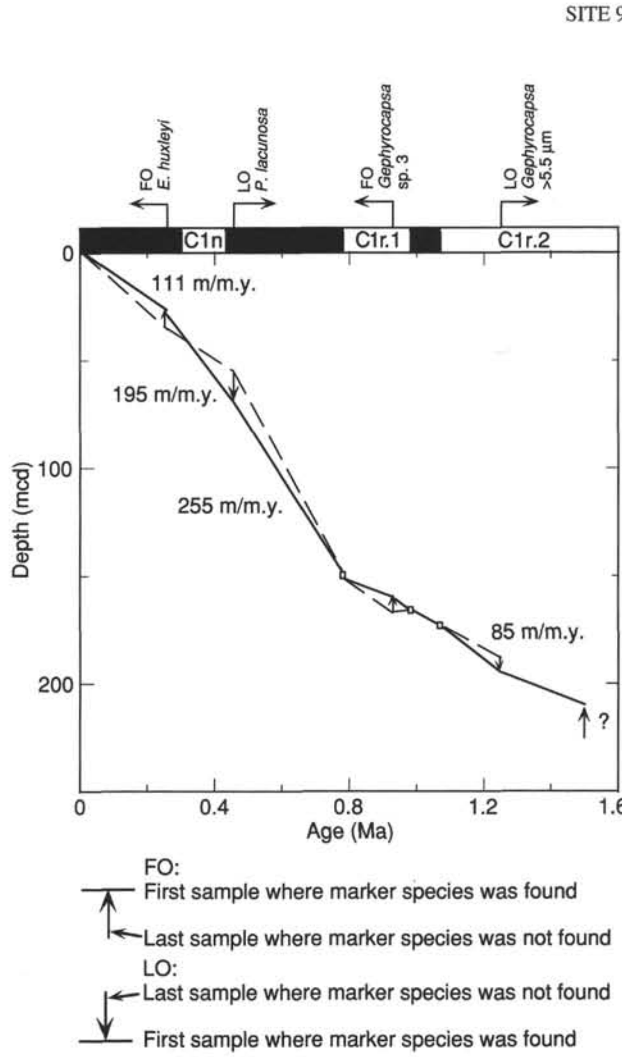

Figure 16. Age vs. depth diagram showing selected calcareous nannofossil datums and paleomagnetic reversals with corresponding sedimentation rates. The core composite depth (mcd) is shown below each fossil datum. The solid line represents the recognized presence/absence of marker species. The dashed line denotes the uncertainty interval.

GRAPE Density

Density was measured in whole cores as part of the MST suite of measurements using the GRAPE (Fig. 32A). GRAPE density shows an overall increase with depth in Hole 963A, and the highest rate of density increase is in the upper 50 m of the core. A comparison of GRAPE density with the wet-bulk density determined from discrete samples shows general agreement, although GRAPE density values are overall lower than index properties bulk density (Fig. 32). A linear correlation exists between GRAPE density and index properties bulk density (Fig. 32B). The systematic mismatch between index properties and GRAPE density values may be explained by the facts that (1) the GRAPE system is calibrated assuming a quartz mineralogy, whereas the dominant lithology of Hole 963A is nannofossil clay, and (2) GRAPE density was measured in undrained whole-round cores in the liner, which have a higher water content than dis-

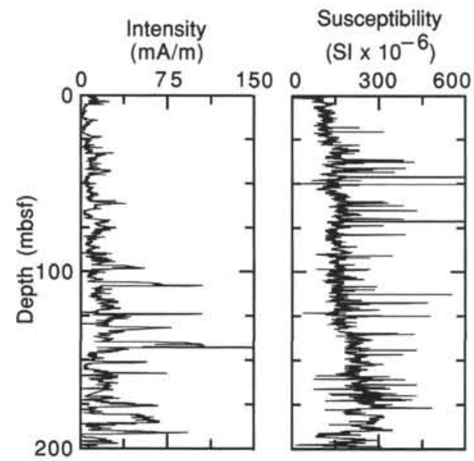

Figure 17. NRM intensity after AF demagnetization at 20 mT and low-field magnetic susceptibility for Hole 963A.

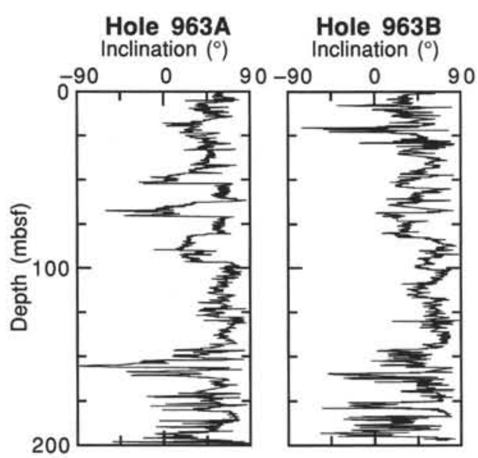

Figure 18. Paleomagnetic inclinations measured on archive core halves using the shipboard pass-through magnetometer for Hole 963A (after AF demagnetization at 20 mT) and Hole 963B (after AF demagnetization at 25 mT). The "hard" overprints evident in Figure 19 indicate that the whole-core inclination logs are contaminated by secondary components of magnetization and that these logs are not reliable for determining a clear magnetostratigraphy.

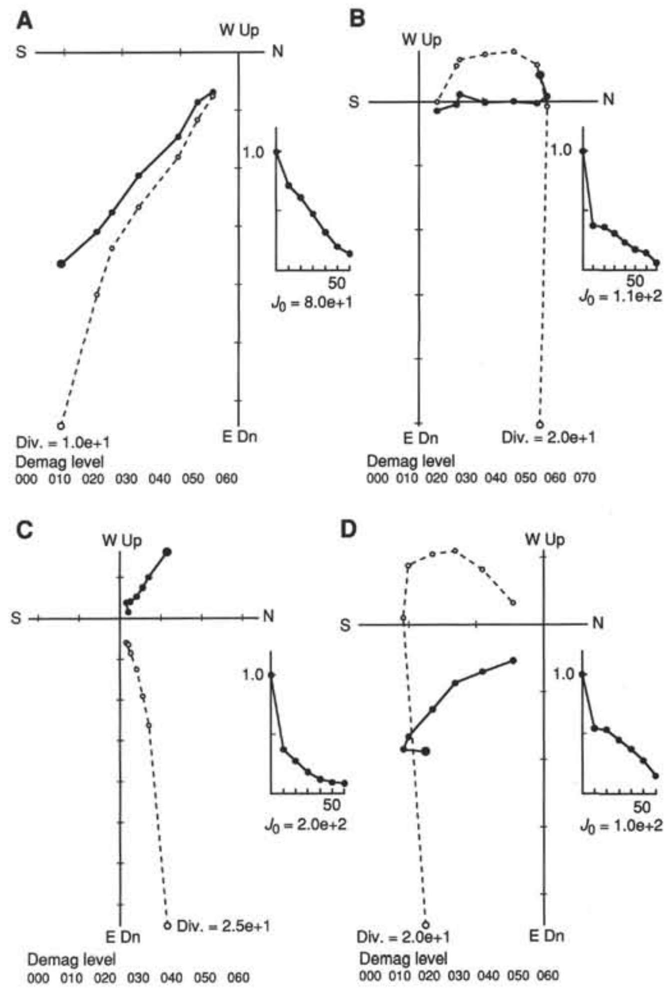

Figure 19. Representative vector component demagnetization diagrams for discrete samples that were subjected to stepwise AF demagnetization. **A.** Sample 160-963A-7H-3, 57 cm (55.57 mbsf); **B.** Sample 160-963A-21H-2, 98 cm (172.98 mbsf); **C.** Sample 160-963A-17H-2, 82 cm (145.42 mbsf); **D.** Sample 160-963A-23H-2, 100 cm (188.50 mbsf). Open (solid) symbols represent projections onto the vertical (horizontal) plane. Demagnetization steps (in mT) are shown below each diagram.

crete index properties samples taken from the partially drained split cores.

Compressional Wave Velocities

Compressional wave velocity was measured parallel and normal to the core axis on split cores from Hole 963A using the digital sound velocimeter system (Table 14, Fig. 33). Velocities generally increase with depth, from 1.5 km/s at the seafloor to 1.6 km/s at 150 mbsf, then the velocity increases to 1.66 at 200 mbsf. Velocity increases sharply in the first 50 m, and increases moderately from 50 to 150 mbsf. Compressional wave velocity increases again in the 150–200 mbsf interval to 1.65 km/s. A similar trend of velocity variation was measured on the MST, although the precision of these measurements is affected by measuring the undrained sediment through the core liner (Fig. 33B). This velocity pattern in Hole 963A is consistent with the measured index properties discussed above. In particular, the downhole distribution of porosity and water content is reflected in the velocity.

Shear Strength

Measurements of shear strength, using a mechanical vane, were made on split cores from Hole 963A, concurrent with the measurement of compressional wave velocity (Table 15, Fig. 34). Reasonable values range from 10 to 250 kPa and generally increase with depth. They increase from 10 to 180 kPa in the upper 35 m. The abrupt porosity and water content increase at this depth (cf., Fig. 31) correlates with a sharp decrease in shear strength. Further compaction results in increasing shear strength to 330 kPa at about 170 mbsf. Below that depth, shear strength decreases despite further compaction. Peak measured shear strength was at 150–170 mbsf, which correlates with a decrease of the water content in the sediments at that interval (Fig. 31).

Magnetic Susceptibility

Magnetic susceptibility was measured within the MST on whole-round cores. Figure 35 shows the distribution of magnetic suscepti-

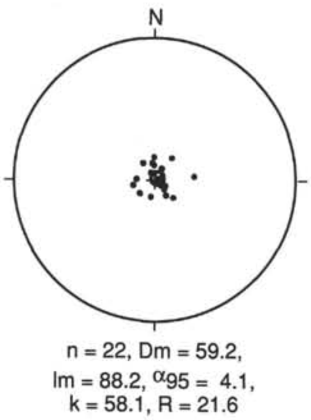

Figure 20. Paleomagnetic directions from the low-coercivity drill-string overprint (determined by linear regression from 0- and 10-mT demagnetization data in vector component plots for n = 22 stepwise-demagnetized discrete samples) plotted on an equal-angle stereographic projection. Symbols represent projections onto the upper hemisphere. Dm = mean inclination, Im = mean inclination, α_{95} = 95% cone of confidence about the mean direction, k = Fisher's precision parameter, and R = sum of each unit vector shown in the figure. The mean direction is statistically indistinguishable from vertical, which is consistent with a soft drill-string-induced overprint.

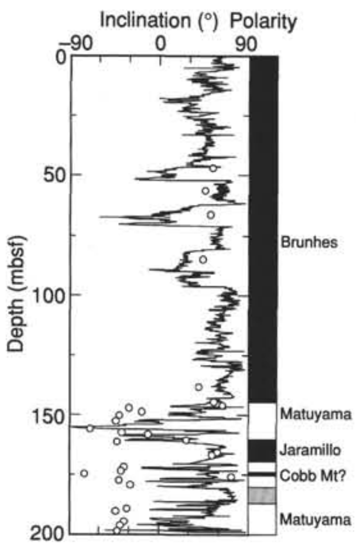

Figure 21. Whole-core inclination for Hole 963A compared with inclinations from stepwise-demagnetized discrete samples. The inclinations for discrete samples were determined by linear regression fits to multiple demagnetization points in each case. These data demonstrate that the whole-core inclination determinations are not useful for defining the magnetostratigraphy for Hole 963A. A preliminary magnetostratigraphic interpretation is shown on the polarity log beside the inclination data (black [white] represents normal [reverse] polarity).

bility with depth for Hole 963A. Owing to compaction and increasing bulk density, the measured values increase with depth. This increase is most pronounced in the upper 50 m. Another steplike increase in susceptibility is at ~135 mbsf. Below that depth, magnetic susceptibility values remain approximately constant, but show more scatter (Fig. 35).

Table 5. Depth of boundaries of magnetic polarity zones in Hole 963A.

Chron boundary	Core, section, interval (cm)	Depth (mbsf)
Base of Brunhes (C1n/C1r.1)	Between 17H-2, 82–84, and 17H-3, 45–47	145.42–146.55
Top of Jaramillo (C1r.1/C1r.1n)	Between 19H-4, 39–41, and 20H-2, 112–114	160.98–165.12
Base of Jaramillo (C1r.1n/C1r.2)	Between 20H-4, 95–97, and 21H-1, 88–90	167.95–171.38

Natural Gamma-ray Radiation

NGR values increase in the first 30 m of the hole and from that depth maintain constant values of approximately 30 counts per second (cps) (Fig. 36). The increase of NGR in the first 30 m of the hole probably results from compaction.

Thermal Conductivity

Thermal conductivity at Hole 963A shows an overall increase with depth, from 1.1 to 1.4 W/(m · K) (Table 16, Fig. 37). The downhole distribution of thermal conductivity correlates with the porosity and water content, which is consistent with the known dependence of density and shear-wave velocity on water content and porosity.

Relationship of Physical Properties to Lithology

In general, the physical properties measured at Hole 963A reflect compaction and diagenetic processes that took place at depths down to 200 mbsf. Detailed observation suggests that compaction is the primary cause for the variation in all the parameters of the physical properties of rocks measured down to a depth of ~30 mbsf (Figs. 31–34). A good correlation exists between *P*-wave velocity, strength, water content, and density; in particular, abrupt changes at 35 and 17 mbsf were observed in all physical properties.

SUMMARY AND CONCLUSIONS

Site 963 at 37°01.94′N, 13°10.89′E, in water 470 m deep is located in the Strait of Sicily and is the westernmost location drilled during Leg 160. The site is on a small, fault-bounded high within the southeastern slope of Adventure Bank. The seafloor forms an embayment off the main channels in the Pantelleria, Linosa, and Malta grabens, which connect the eastern and western Mediterranean basins. Seismic reflection profiles suggest that the Pliocene-Quaternary sediments here are 200 to 300 m thick and overlie a prominent, highly disrupted acoustic reflector of unknown age. Because of shallow water depths and safety considerations, penetration at Site 963 was restricted to 200 mbsf.

The primary scientific objective at Site 963 was to clarify the history of water exchange between the two Mediterranean sub-basins. The seafloor at Site 963 is in the water depth interval occupied by westward-flowing Mediterranean Intermediate Water, which forms in the Eastern Mediterranean from the sinking of warm, saline, oxygen-rich water. Variations in sediment properties and in the benthic record on the sill reflect changes in the Mediterranean circulation system, and specifically in the character of MIW.

A second important objective at the site was to correlate the submarine sedimentary record to well-studied land sections of uplifted Pliocene to middle Pleistocene sediments that are exposed in southern Sicily and in Calabria. We aimed to bridge the stratigraphic gap between the youngest (i.e., lower Pleistocene) sapropels exposed on

Table 6. Structural data collected at Site 963.

Core, section, interval (cm)	Depth (mbsf)	Feature	Offset width (cm)	Orientation on core face (degrees) Apparent dip	Direction	Second apparent direction (degrees) Apparent dip	Direction	Calculated orientation (degrees) Dip	Direction	Geographic orientation (degrees) Dip	Direction	Comments
160-963A-												
3H-4, 27–32	18.77	SB/C		7	90	3	0	8	67			Slightly dipping silt bed
3H-5, 55–61	20.55	SB/C		0								Ash/turbidite?, dark gray fining upward, subhorizontal
4H-2, 132–142	26.32	SB/C		0								Indurated silt, subcentimeter fragments up to 3 cm in diameter, fining upward.
4H-3, 117–121	27.67	SB/C		0								Dark gray silt, irregular contact at base
4H-5, 90–110	30.4	SB/C		0								Horizontal bedding due to faint changes in color and/or enrichment in pyrite
4H-5, 130–140	30.8	SB/C		0								Coarse-grained sediments (turbiditic?)
5H-4, 5–14	37.55	SB/C		0								Coarse-grained sediments (turbiditic?)
6H-5, 16	48.66	SB/C		0								Subhorizontal sedimentary bedding
5H-5, 54–55	39.54	SB/C		0								Dark-gray color
5H-5, 109–110	40.09	SB/C		0								Dark-gray color
5H-6, 74–79	41.24	SB/C		3	90	2	0	4	56	4	279	Coarse silt/ash, dark gray base, slightly fining upward
6H-3, 56–73	46.06	SB/C		25	270	35	0	40	326	40	6	Ash/turbidite?
6H-5, 40	48.9	SB/C		0								Yellow laminations
6H-5, 43	48.93	SB/C		0								Subhorizontal sedimentary bedding
6H-5, 103	49.53	SB/C		0								Subhorizontal sedimentary bedding
6H-5, 120	49.7	SB/C		0								Subhorizontal sedimentary bedding
6H-6, 24–26	50.24	SB/C		0								Subhorizontal sedimentary bedding
6H-6, 84–87	50.84	SB/C		0								Subhorizontal sedimentary bedding
6H-CC, 7–8	52.14	SB/C		0								Subhorizontal sedimentary bedding
8H-1, 93–95	62.43	SB/C		0								Subhorizontal sedimentary bedding
8H-3, 55–57	65.05	SB/C		0								Subhorizontal sedimentary bedding
8H-6, 43–44	69.43	SB/C		0								Subhorizontal sedimentary bedding
8H-CC, 33–36	71	SB/C		?								Kinked base of gray silt (drilling disturbance?)
9H-4, 51–52	76.01	SB/C		0								Subhorizontal sedimentary bedding
9H-6, 6–6	78.56	SB/C		0								Subhorizontal sedimentary bedding
9H-6, 30–44	78.8	SB/C		0								Subhorizontal sedimentary bedding
9H-6, 82–83	79.32	SB/C		0								Subhorizontal sedimentary bedding
9H-6, 88–88	79.38	SB/C		0								Subhorizontal sedimentary bedding
9H-6, 132–132	79.82	SB/C		0								Subhorizontal sedimentary bedding
10H-3, 72–73	84.22	SB/C		0								Subhorizontal sedimentary bedding
10H-4, 92–93	85.92	SB/C		0								Subhorizontal sedimentary bedding
10H-4, 96–97	85.96	SB/C		0								Subhorizontal sedimentary bedding
11H-1, 0–60	90	?FR		90								More likely a burrow
12H-1, 93–99	99.53	SB/C		0								Subhorizontal sedimentary bedding
12H-4, 82–85	103.92	SB/C		0								Subhorizontal sedimentary bedding
13H-2, 48–50	110.08	SB/C		0								Subhorizontal sedimentary bedding
14H-1, 5	115.15	SB/C		0								Subhorizontal sedimentary bedding
14H-1, 29–36	115.39	SB/C		0								Subhorizontal sedimentary bedding
14H-1, 70–72	115.8	SB/C		0								Subhorizontal sedimentary bedding
15H-3 , 78–82	128.6	SB/C		0								Subhorizontal sedimentary bedding
15H-3, 100	128.38	SB/C		0								Subhorizontal sedimentary bedding
15H-4, 52–70	129.62	SB/C		0								Subhorizontal sedimentary bedding
22H-1, 31–32	176.81	SB/C		0								Subhorizontal sedimentary bedding
22H-2, 17–23	178.17	F		80	270	0	20	81	290	81	63	Small normal fault structures offsetting nearly horizontal color changes (probably bedding)
22H-2, 114–115	179.14	SB/C		0								Subhorizontal sedimentary bedding
23H-1, 15–16	186.15	SB/C		0								Subhorizontal sedimentary bedding
23H-2, 8	187.58	SB/C		0								Subhorizontal sedimentary bedding
23H-2, 10	187.6	SB/C		0								Subhorizontal sedimentary bedding
23H-2, 14	187.64	SB/C		0								Subhorizontal sedimentary bedding
23H-2, 15	187.65	SB/C		0								Subhorizontal sedimentary bedding
23H-2, 17	187.67	SB/C		0								Subhorizontal sedimentary bedding
24H-1, 17–18	192.17	SB/C		0								Subhorizontal sedimentary bedding
24H-2, 71	194.21	SB/C		0								Subhorizontal sedimentary bedding
24H-2, 76	194.26	SB/C		0								Subhorizontal sedimentary bedding
24H-2, 119	194.69	SB/C		0								Subhorizontal sedimentary bedding
24H-2, 126	194.76	SB/C		0								Subhorizontal sedimentary bedding
24H-3, 23–24	195.23	SB/C		18								Subhorizontal sedimentary bedding
160-963B-												Subhorizontal sedimentary bedding
1H-3, 52–60	3.52	SB		48	90	90	0	48	90			Change in color, slumping?
1H-5, 49	6.49	SB	0									Yellowish gray
1H-5, 137	7.37	SB	0									Yellowish gray

Table 6 (continued).

Core, section, interval (cm)	Depth (mbsf)	Feature	Offset width (cm)	Orientation on core face (degrees) Apparent dip	Direction	Second apparent direction (degrees) Apparent dip	Direction	Calculated orientation (degrees) Dip	Direction	Geographic orientation (degrees) Dip	Direction	Comments
3H-3, 28–41	21.78	SB		24	90	0	170	24	80			Ash; sharp horizontal basal contact
3H-7, 18–37	27.68	SP		24	270	28	180	35	220			Basal contact of slump
7H-5, 14–21	62.64	SB		2	90	21	180	21	175			Top of coarse-grained ash layer
9H-5, 30–45	79.3	SB		82	90	5	0	82	89			Subhorizontal sedimentary bedding
10H-3, 110–150	86.6	F	8	75	90	27	0	75	82			Normal fault, offset is approximate
16H-1, 134–143	137.24	F	2	80	270	72	0	81	298			Syn-sedimentary normal fault, offset is approximate
18H-3, 84–109	152.74	F	0.5	74	270							Normal fault, offset is approximate
19H-3, 107–110	162.47	F	1	56	90							Normal fault, offset is approximate
21H-1, 80–90	175.7	F?										Linear feature crosscutting the core, but not visible in either the 0° dip plane or in the 360°–180° plane
22H-4, 63–69	188.53	F	1	42	270	34	0	48	307			Normal fault, offset is approximate

Note: Feature symbols defined in Table 2 ("Explanatory Notes" chapter, this volume).

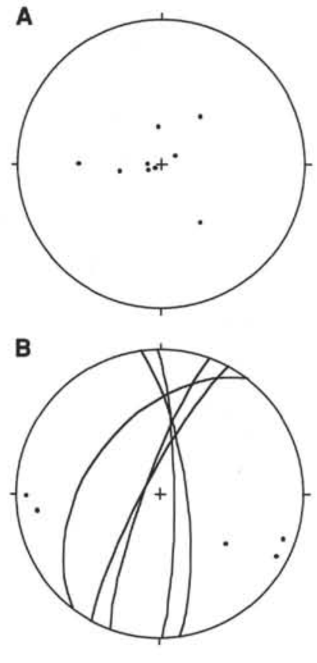

Figure 22. **A.** Equal-area lower hemisphere projection of poles to bedding plotted with respect to the core reference frame. **B.** Great circles and poles to planes of normal faults with respect to the core reference frame.

land and the late Pleistocene age marine sapropel record of the eastern Mediterranean Sea.

Three holes were drilled at Site 693 in APC mode; in addition, we sampled a mud-line core in Hole 963D (0–8.4 mbsf). Recovery and core quality in the four APC holes was excellent (average recovery 101%) and yielded a complete sediment section that spans the lower Pleistocene to the Holocene. Hole 963A was cored to 199.4 mbsf and recovered 203.1 m, Hole 963B was cored to 204.5 mbsf and recovered 206.2 m, and Hole 963C was cored to 57.0 mbsf and recovered 57.9 m. Detailed records of magnetic susceptibility and density were generated on the shipboard multisensor track to facilitate core correlation and to ensure that a complete record was recovered. These high-resolution records were supplemented with measurements of color reflectance on split-core surfaces.

The sediments of the one sedimentary unit are olive-green nannofossil clays with minor quartzose silt and volcanic ash. At the base, we found layers enriched in organic carbon. Six discrete, thin-bedded and graded ash layers (<18 cm) were recognized in the upper 100 m. The nannofossil clay of the upper section is homogeneous to locally bioturbated and rich in calcareous microfossils. In the uppermost section (at approximately 5 mbsf), the color changes from brownish gray to light olive green/gray. Below 125 mbsf, a series of increasingly darker colored layers 10 to 50 cm thick occur. The two darkest of these layers were found at the base of the section and are distinctly laminated on a millimeter scale. In the section below 125 mbsf, the amplitudes of cyclic variations in the physical properties (monitored by the MST, reflectance, and color data) increase significantly. The carbonate content of the sediment varies between 20% and 45% by weight, and organic carbon values are between 0.1% and 1.5%, with maximal values occurring in the dark layers in the lower part of the section. The organic matter is hydrogen poor and appears to be degraded. The pore-water and interstitial gas concentrations suggest that the diagenesis of organic matter is only moderate; methane concentrations remain below 300 μL/L where sulfate is present only in trace amounts (60 mbsf). Depth profiles of dissolved ions indicate carbonate precipitation in the sediment and require a source of sulfate and calcium at depth. Some small high-angle normal faults (offset on

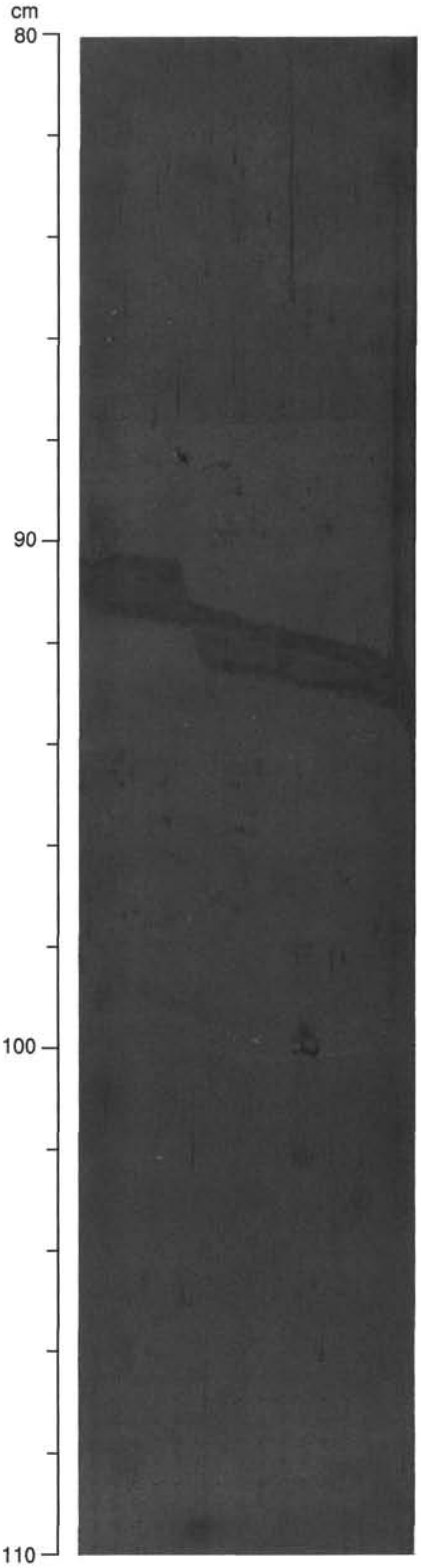

Figure 23. Curving steep microfault in Section 160-963B-18H-3, 80–110 cm. Note the 1-cm offset of the shallowly dipping dark layer (probably burrows) between 90 and 93 cm.

Table 7. Site 963 composite depth section.

Core	Depth (mbsf)	Offset (m)	Depth (mcd)
160-963A-			
1H	0.00	0.03	0.03
2H	4.50	1.60	6.10
3H	14.00	2.09	16.09
4H	23.50	2.18	25.68
5H	33.00	3.09	36.09
6H	42.50	3.60	46.10
7H	52.00	3.99	55.99
8H	61.50	3.60	65.10
9H	71.00	3.60	74.60
10H	80.50	3.60	84.10
11H	90.00	3.40	93.40
12H	98.60	3.40	102.00
13H	108.10	3.40	111.50
14H	115.10	3.40	118.50
15H	124.60	3.81	128.41
16H	133.60	3.81	137.41
17H	143.10	3.81	146.91
18H	151.50	3.81	155.31
19H	156.50	3.41	159.91
20H	162.50	3.81	166.31
21H	170.50	3.81	174.31
22H	176.50	4.32	180.82
23H	186.00	4.32	190.32
24H	192.00	4.32	196.32
25H	197.50	4.32	201.82
160-963B-			
1H	0.00	0.00	0.00
2H	9.00	0.00	9.00
3H	18.50	0.81	19.31
4H	28.00	2.79	30.79
5H	37.50	2.30	39.80
6H	47.00	2.61	49.61
7H	56.50	3.39	59.89
8H	66.00	3.39	69.39
9H	75.50	3.00	78.50
10H	82.50	3.00	85.50
11H	92.00	2.59	94.59
12H	100.70	2.40	103.10
13H	108.90	2.29	111.19
14H	116.90	3.00	119.90
15H	126.40	3.91	130.31
16H	135.90	4.01	139.91
17H	142.10	3.62	145.72
18H	148.90	3.62	152.52
19H	158.40	3.62	162.02
20H	165.40	3.62	169.02
21H	174.90	3.22	178.12
22H	183.40	5.24	188.64
23H	189.90	4.43	194.33
24H	197.50	4.43	201.93
160-963C-			
1H	0.00	0.21	0.21
2H	9.50	–0.79	8.71
3H	19.00	0.21	19.21
4H	28.50	0.21	28.71
5H	38.00	1.40	39.40
6H	47.50	2.01	49.51
160-963D-			
1H	0.00	0.25	0.25

a scale of centimeters) were observed below 100 mbsf. The faults may reflect tectonic instability in the underlying basement or disturbance induced by compaction and slumping.

The sequence at Site 963 spans the time interval from the early Pleistocene (1.5 Ma) to the Holocene at an extraordinary resolution. Age assignments are based on calcareous nannofossil assemblage datums supplemented by planktonic foraminifers and on a preliminary paleomagnetic reversal stratigraphy. According to the shipboard assessment, the sediment section is complete and was deposited at rates between 85 m/m.y. in the section below 150 m and up to 250 m/m.y. in the interval between 150 and 50 mbsf; rates in the upper part of the section are estimated at 110 m/m.y. The high rates of sedimentation may be a result of tectonic subsidence in the middle Pleistocene and may be related to flexural depression of the crust as a result of earlier (pre-early Pleistocene) nappe emplacement on the unstable foreland of North Africa.

Calcareous nannofossils are well preserved and the assemblage is characterized by considerable admixtures of reworked species from

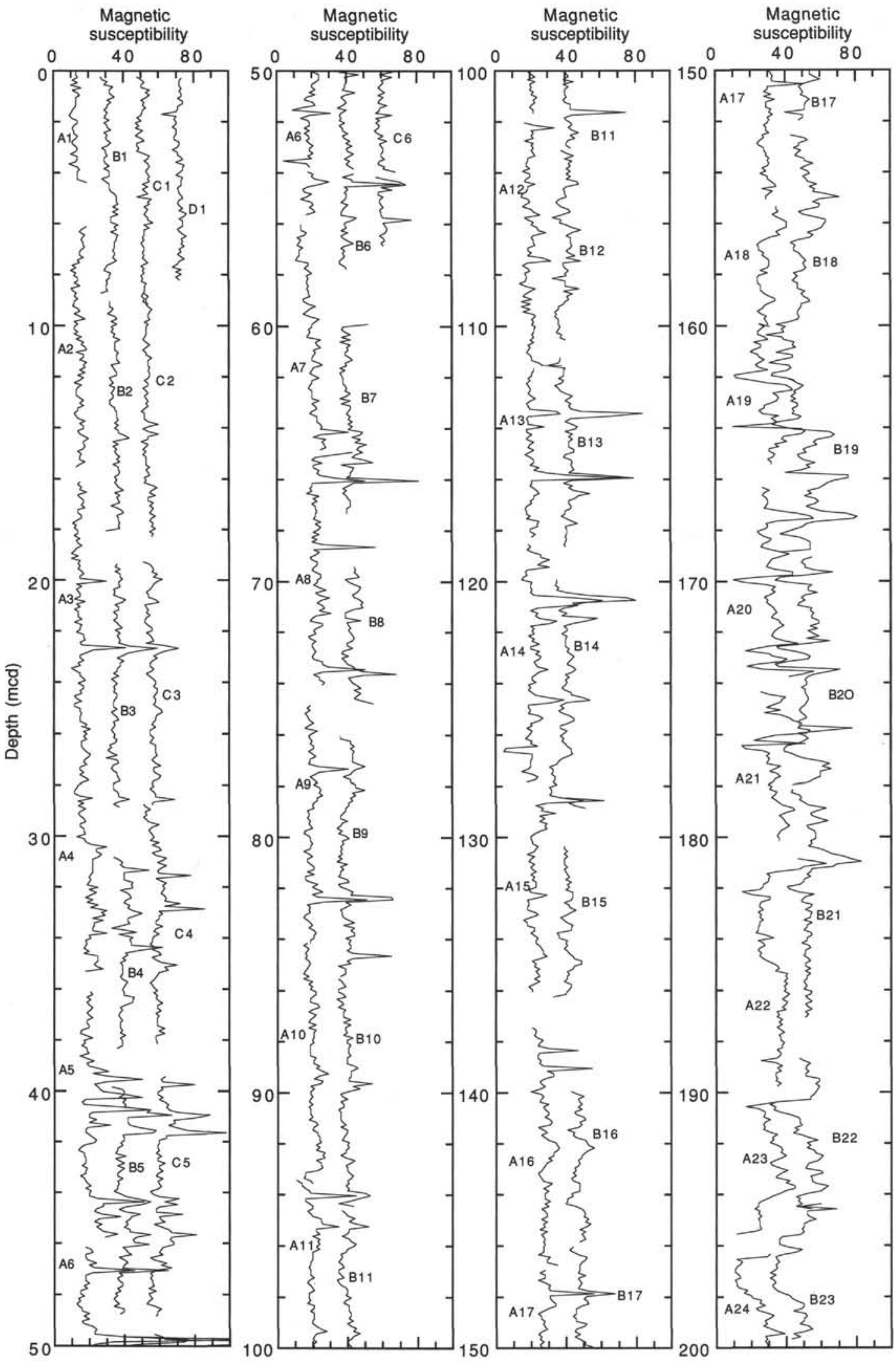

Figure 24. Magnetic susceptibility data (uncorrected instrument units) from Site 963 on the mcd (meters composite depth) scale. Holes 963A through 963D are offset from each other by a constant (20 instrument units). Cores for each hole are shown (e.g., B3 = Core 160-963B-3H).

Table 8. Site 963 splice tie points.

Hole, core, section, interval (cm)	Depth (mbsf)	Depth (mcd)		Hole, core, section, interval (cm)	Depth (mbsf)	Depth (mcd)
963B-1H-6, 34.4	7.84	7.84	ties to	963A-2H-2, 24.5	6.24	7.84
963A-2H-5, 134.5	11.85	13.45	ties to	963B-2H-3, 104.5	13.05	13.45
963B-2H-6, 104.6	17.05	17.45	ties to	963A-3H-1, 64.4	14.64	17.45
963A-3H-5, 54.4	20.54	23.35	ties to	963B-3H-3, 34.4	21.84	23.35
963B-3H-7, 24.6	27.75	29.26	ties to	963A-4H-2, 134.4	26.34	29.26
963A-4H-6, 144.5	32.44	35.36	ties to	963C-4H-5, 4.5	34.54	35.36
963C-4H-6, 144.5	37.44	38.26	ties to	963A-5H-2, 34.4	34.84	38.26
963A-5H-6, 74.6	41.25	44.67	ties to	963B-5H-4, 4.5	42.04	44.67
963B-5H-5, 124.4	44.74	47.37	ties to	963A-6H-1, 94.5	43.44	47.37
963A-6H-6, 24.4	50.24	54.17	ties to	963B-6H-3, 134.6	51.35	54.17
963B-6H-5, 114.5	54.15	56.97	ties to	963A-7H-1, 44.4	52.44	56.97
963A-7H-6, 64.5	60.15	64.68	ties to	963B-7H-3, 114.5	60.65	64.68
963B-7H-5, 14.5	62.65	66.68	ties to	963A-8H-1, 94.5	62.44	66.68
963A-8H-6, 84.4	69.84	74.08	ties to	963B-8H-4, 74.5	70.23	74.08
963B-8H-5, 114.6	71.38	75.23	ties to	963A-9H-1, 4.4	71.04	75.23
963A-9H-6, 34.4	78.84	83.03	ties to	963B-9H-5, 44.5	79.44	83.03
963B-9H-7, 34.4	82.34	85.93	ties to	963A-10H-1, 134.6	81.85	85.93
963A-10H-4, 114.5	86.14	90.22	ties to	963B-10H-4, 4.5	87.04	90.22
963B-10H-6, 104.5	91.04	94.22	ties to	963A-11H-1, 64.5	90.64	94.22
963A-11H-2, 34.4	91.84	95.42	ties to	963B-11H-1, 64.6	92.65	95.42
963B-11H-5, 104.6	99.05	101.82	ties to	963A-12H-1, 24.6	98.85	101.82
Append Core 160-963A-13H to Core 160-963A-12H						
Append Core 160-963A-14H to Core 160-963A-13H						
963A-14H-5, 14.4	121.24	124.64	ties to	963B-14H-4, 24.5	121.65	124.64
963B-14H-6, 114.6	125.55	128.54	ties to	963A-15H-1, 14.4	124.74	128.54
Append Core 160-963A-16H to Core 160-963A-15H						
963A-16H-6, 144.4	142.54	146.35	ties to	963B-17H-1, 24.5	142.64	146.35
963B-17H-2, 124.4	145.14	148.85	ties to	963A-17H-2, 24.4	144.84	148.85
963A-17H-4, 144.5	149.05	153.06	ties to	963B-18H-1, 54.5	149.44	153.06
963B-18H-7, 44.5	158.35	161.97	ties to	963A-19H-2, 104.5	158.63	161.97
963A-19H-3, 144.5	160.54	163.88	ties to	963B-19H-2, 34.4	160.24	163.88
963B-19H-4, 94.6	163.85	167.49	ties to	963A-20H-1, 124.6	163.75	167.49
963A-20H-5, 104.4	169.54	173.28	ties to	963B-20H-3, 124.5	169.64	173.28
963B-20H-5, 74.6	172.15	175.79	ties to	963A-21H-2, 4.5	172.04	175.79
963A-21H-4, 24.5	175.14	178.89	ties to	963B-21H-1, 74.4	175.64	178.89
963B-21H-3, 84.5	178.74	181.99	ties to	963A-22H-1, 134.4	177.84	181.99
Append Core 160-963A-23H to Core 160-963A-22H						
963A-23H-4, 64.4	191.14	195.46	ties to	963B-23H-1, 114.6	191.05	195.46
963B-23H-3, 24.5	193.14	197.55	ties to	963A-24H-1, 114.5	193.15	197.55
Append Core 160-963A-25H to Core 160-963A-24H						

Table 9. Results of pore-water analyses for Site 963.

Core, section, interval (cm)	pH	Alkalinity (meq/L)	Salinity (g/kg)	Cl^- (mM)	Mg^{2+} (mM)	Ca^{2+} (mM)	SO_4^{2-} (mM)	NH_4^+ (μM)	SiO_2 (μM)	K^+ (mM)	Br^- (mM)	Li^+ (μM)	Na (mM)
160-963A-													
2H-5, 145–150	7.35	3.658	36.0	609	48.20	8.32	15.60	1250	227	10.11	1.02	49	517
3H-5, 145–150	7.34	4.382	36.0	607	44.42	7.30	8.20	1405	216	9.32	1.05	49	509
6H-5, 145–150	7.38	4.992	34.0	602	38.91	6.42	0.90	1505	212	8.94	1.06	57	516
9H-5, 145–150	7.54	4.613	34.0	597	36.52	6.49	0.25	1645	247	8.21	1.15	57	503
12H-5, 140–150	7.41	4.637	34.0	597	37.11	6.65	0.30	1725	266	7.42	1.10	58	515
15H-4, 140–150	7.58	5.253	33.0	597	36.60	6.08	0.60	1770	199	7.81	1.02	66	497
18H-2, 140–150	7.60	7.014	33.5	602	37.62	5.14	0.35	1820	227	7.73	1.01	79	494
21H-3, 140–150	7.46	6.750	34.0	602	38.94	5.97	2.80	1875	234	7.95	0.91	91	494
24H-2, 140–150	7.41	4.808	34.0	603	37.49	9.50	7.30	1830	275	7.72	1.04	100	539
160-963D-													
1H-1, 145–150	7.45	4.796	38.0	622	59.27	10.65	28.40	285	192	11.19	1.08	32	528
1H-3, 145–150	7.34	4.430	38.0	618	55.23	9.58	25.10	610	184	11.22	1.24	41	533
1H-5, 145–150	7.80	4.880	37.0	618	52.15	8.94	22.10	855	140	11.23	1.16	45	513

Pliocene, Miocene, Eocene, and Upper Cretaceous strata exposed on land and at the seafloor in the vicinity of Adventure Bank. The planktonic foraminifer assemblage shows no significant reworking and is well preserved. Benthic foraminifers are present throughout the section, radiolaria are rare, and diatoms are absent.

The paleomagnetic record of Site 963 extends into the Matuyama Chron and the Jaramillo Subchron is clearly present. In addition, several short intervals of anomalous magnetization are evident in the Brunhes Chron.

Site 963 achieved both objectives: we recovered a complete and highly resolved sedimentary record with high stratigraphic potential (physical properties, biostratigraphy, magnetostratigraphy, and stable isotope stratigraphy) and we were able to recover lower Pleistocene organic-rich intervals that shore-based research will tie to the occurrences of sapropels in land sections.

REFERENCES

Argnani, A., 1989. The Gela Nappe: evidence of accretionary melange in the Maghrebian foredeep of Sicily. *Mem. Soc. Geol. Ital.*, 38:419–428.

Béthoux, J.-P., 1989. Oxygen consumption, new production, vertical advection and environmental evolution of the Mediterranean Sea. *Deep-Sea Res.*, 36:769–781.

Brumsack, H.-J., Zuleger, E., Gohn, E., and Murray, R.W., 1992. Stable and radiogenic isotopes in pore waters from Leg 127, Japan Sea. *In* Pisciotto, K.A., Ingle, J.C., Jr., von Breymann, M.T., Barron, J., et al., *Proc. ODP, Sci. Results,* 127/128 (Pt. 1): College Station, TX (Ocean Drilling Program), 635–650.

Catalano, R., Di Stefano, P., Nigro, F., and Vitale, F.P., 1993a. Sicily mainland and its offshore: a structural comparison. *In* Max, M.D., and Colantoni, P. (Eds.), *Geological Development of the Sicilian-Tunisian Platform.* UNESCO Rep. Mar. Sci., 58:19–24.

Catalano, R., Infuso, S., and Sulli, A., 1993b. The Pelagian Foreland and its northward foredeep: Plio-Pleistocene structural evolution. *In* Max, M.D., and Colantoni, P. (Eds.), *Geological Development of the Sicilian-Tunisian Platform.* UNESCO Rep. Mar. Sci., 58:37–42.

Di Stefano, E., Infuso, S., and, Scarantino, S., 1993. Plio-Pleistocene sequence stratigraphy of western offshore Sicily from well logs and seismic sections in a high-resolution calcareous plankton biostratigraphic framework. *In* Max, M.D., and Colantoni, P. (Eds.), *Geological Development of the Sicilian-Tunisian Platform.* UNESCO Rep. Mar. Sci., 58:37–42.

Di Stefano, E., and Sprovieri, R., 1990. Calcareous plankton biostratigraphy of ODP Leg 107 Site 651, uppermost Pliocene–lowermost Pleistocene. *Mem. Soc. Geol. Ital.,* 44:157–165.

Emelyanov, E., 1972. Principal types of recent bottom sediments in the Mediterranean Sea: their mineralogy and geochemistry. *In* Stanley, D. (Ed.), *The Mediterranean Sea: A Natural Sedimentation Laboratory:* Stroudsburg, PA (Dowden, Hutchinson and Ross), 355–386.

Gieskes, J.M., 1981. Deep-sea drilling interstitial water studies: implications for chemical alteration of the oceanic crust, layers I and II. *In* Warme, J.E., Douglas, R.G., and Winterer, E.L. (Eds.), *The Deep Sea Drilling Project: A Decade of Progress.* Spec. Publ.—Soc. Econ. Paleontol. Mineral., 32:149–167.

————, 1983. Interstitial waters of deep sea sediments. *In* Chester, J.P., and Riley, R. (Eds.), *Chemical Oceanography* (Vol. 6): New York (Academic), 221–269.

Kemp, A.E.S., 1995. Variation of trace fossils and ichnofacies in Neogene and Quaternary pelagic sediments from the eastern equatorial Pacific Ocean (Leg 138). *In* Pisias, N.G., Mayer, L.A., Janecek, T.R., Palmer-Julson, A., and van Andel, T.H. (Eds.), *Proc. ODP, Sci. Results,* 138: College Station, TX (Ocean Drilling Program), 177–190.

Ludden, J.N., Gradstein, F.M., et al., 1990. *Proc. ODP, Init. Repts.,* 123: College Station, TX (Ocean Drilling Program).

Manheim, F.T., and Sayles, F.L., 1974. Composition and origin of interstitial waters of marine sediments based on deep sea drill cores. *In* Goldberg, E.D. (Ed.), *The Sea* (Vol. 5): New York (Wiley Interscience), 527–568.

Milliman, J., and Müller, J., 1973. Precipitation and lithification of magnesian calcite in the deep-sea sediments of the eastern Mediterranean. *Sedimentology,* 20:29–45.

Ruggieri, G., and Sprovieri, R., 1977. A revision of Italian Pleistocene stratigraphy. *Geol. Rom.,* 16:131–139.

Sarmiento, J., Herbert, T., and Toggweiler, J., 1988. Mediterranean nutrient balance and episodes of anoxia. *Global Biogeochem. Cycles,* 2:427–444.

Stanley, D. (Ed.), 1972. *The Mediterranean Sea: A Natural Sedimentation Laboratory:* Stroudsburg, PA (Dowden, Hutchinson and Ross).

Trincardi, F., and Argnani, A., 1990. Gela submarine slide: a major basin-wide event in the Plio-Quaternary foredeep of Sicily. *Geo-Mar. Lett.,* 10:13–21.

Ms 160IR-104

NOTE: Core-description forms ("barrel sheets") and core photographs can be found in Section 5, beginning on page 535. Forms containing smear-slide data can be found in Section 6, beginning on page 951. Color reflectance, physical properties, chemistry, and thin-section data are presented on the CD-ROM (back pocket).

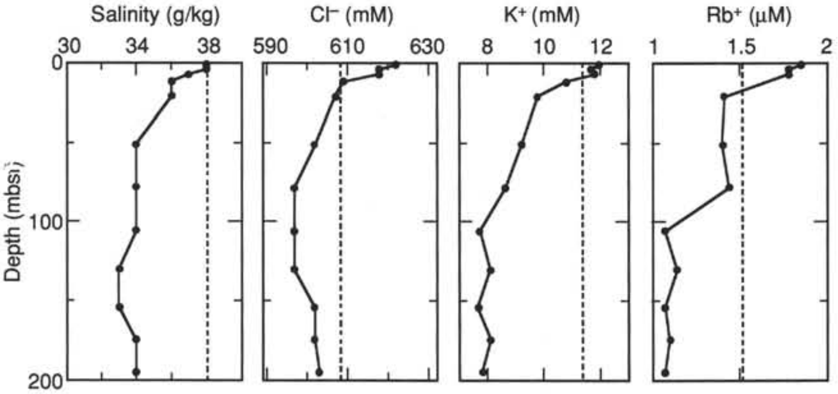

Figure 25. Pore-water vs. depth profiles in Hole 963A for salinity, chloride, potassium, and rubidium. The dashed line indicates the bottom-water concentration.

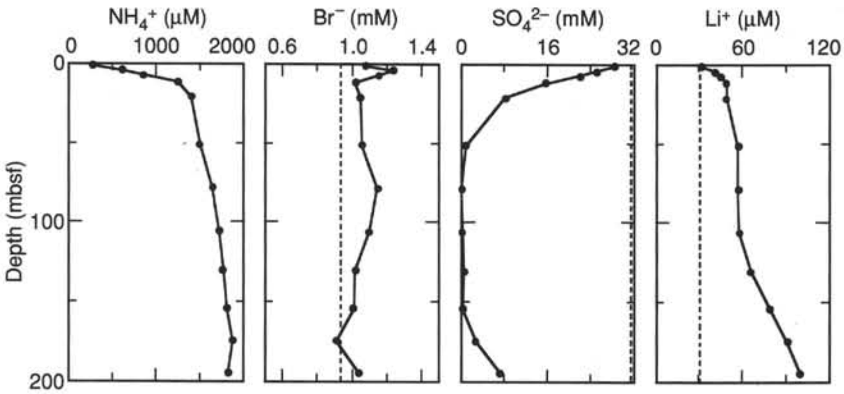

Figure 26. Pore-water vs. depth profiles in Hole 963A for ammonium, bromide, sulfate, and lithium. The dashed line indicates the bottom-water concentration; the ammonium bottom-water concentration is <1 µM.

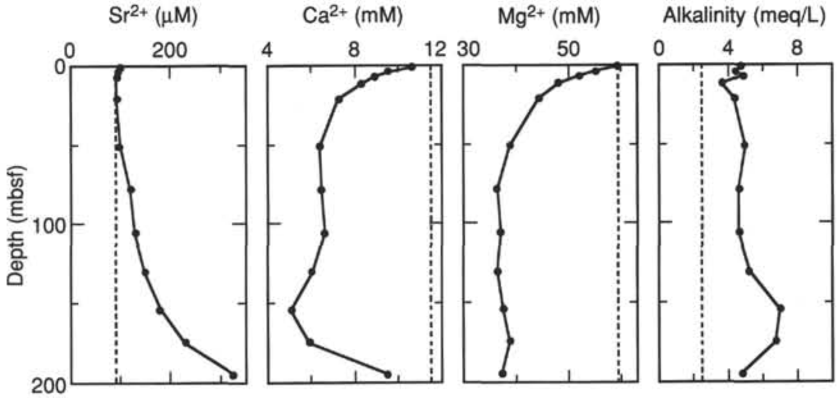

Figure 27. Pore-water vs. depth profiles in Hole 963A for strontium, calcium, magnesium, and alkalinity. The dashed line indicates the bottom-water concentration.

Table 10. Hydrocarbon gas data for Site 963, headspace method.

Core, section, interval (cm)	Depth (mbsf)	C_1 (ppm)
160-963A-		
1H-3, 0–5	3.00	3
2H-6, 0–5	12.00	3
3H-6, 0–5	21.50	3
4H-6, 0–5	31.00	3
5H-6, 0–5	40.50	4
6H-6, 0–5	50.00	3
7H-6, 0–5	59.50	4
8H-6, 0–5	69.00	86
9H-6, 0–5	78.50	270
10H-6, 0–5	88.00	118
11H-5, 0–5	96.00	82
12H-6, 0–5	106.10	82
13H-5, 0–5	114.10	95
14H-6, 0–5	122.60	180
15H-5, 0–5	130.60	122
16H-6, 0–5	141.10	76
17H-5, 0–5	149.10	50
18H-3, 0–5	154.50	24
19H-4, 0–5	160.59	13
20H-5, 0–5	168.50	11
21H-4, 0–5	174.90	7
22H-6, 0–5	184.00	6
23H-3, 0–5	189.00	4
24H-3, 0–5	195.00	3
25H-1, 0–5	197.50	2

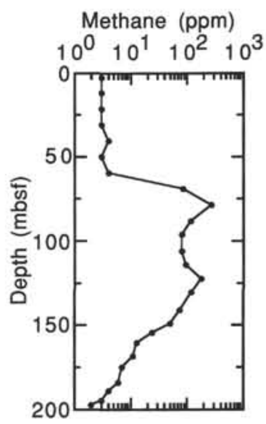

Figure 28. Downhole distribution of methane in sediments at Hole 963A.

Table 11. Concentration of total, inorganic, and organic carbon, calcium carbonate, total nitrogen, and sulfur in sediments from Site 963.

Core, section, interval (cm)	Depth (mbsf)	Total carbon (%)	Inorganic carbon (%)	Organic carbon (%)	$CaCO_3$ (%)	Nitrogen (%)	Sulfur (%)	C_{org}/N	C_{org}/S
160-963A-									
1H-2, 69–70	2.19	3.21	2.75	0.46	22.9	0.09	0.08	5.4	5.5
1H-3, 70–71	3.70		3.19		26.6				
2H-2, 70–71	6.70		2.29		19.1				
2H-4, 71–72	9.71		2.53		21.1				
2H-6, 70–71	12.70		2.48		20.7				
3H-2, 71–72	16.21		2.41		20.1				
3H-4, 71–72	19.21	2.71	2.47	0.24	20.6	0.08	0.04	3.1	5.9
3H-6 , 71–72	22.21		2.37		19.7				
4H-2, 71–72	25.71		2.51		20.9				
4H-4, 71–72	28.71	2.81	2.58	0.23	21.5	0.07	0.02	3.2	11.6
4H-6, 71–72	31.71		2.64		22.0				
5H-2, 70–71	35.20		2.47		20.6				
5H-4, 70–71	38.20	2.74	2.56	0.18	21.3	0.07	0.06	2.5	3.2
5H-6, 70–71	41.20		2.37		19.7				
6H-2, 70–71	44.70		2.10		17.5				
6H-4, 70–71	47.70	2.92	2.63	0.29	21.9	0.08	0.07	3.6	3.9
6H-6, 70–71	50.70		2.29		19.1				
7H-2, 71–72	54.21		2.55		21.2				
7H-4, 71–72	57.21	2.77	2.52	0.25	21.0	0.07	0.00	3.4	
7H-6, 71–72	60.21		2.74		22.8				
8H-2, 71–72	63.71		2.83		23.6				
8H-4, 70–71	66.70	2.87	2.65	0.22	22.1	0.08	0.00	2.9	
8H-6, 71–72	69.71		2.52		21.0				
9H-2, 70–71	73.20		2.23		18.6				
9H-4, 70–71	76.20	2.84	2.56	0.28	21.3	0.08	0.06	3.3	5.0
9H-6, 70–71	79.20		2.49		20.7				

Table 11 (continued).

Core, section, interval (cm)	Depth (mbsf)	Total carbon (%)	Inorganic carbon (%)	Organic carbon (%)	$CaCO_3$ (%)	Nitrogen (%)	Sulfur (%)	C_{org}/N	C_{org}/S
10H-2, 70–71	82.70		2.72		22.7				
10H-4, 70–71	85.70	3.33	3.19	0.14	26.6	0.07	0.06	1.9	2.2
10H-6, 70–71	88.70		2.83		23.6				
11H-2, 70–71	92.20		3.66		30.5				
11H-4, 70–71	95.20	3.29	3.00	0.29	25.0				
11H-6, 70–71	98.20		2.55		21.2				
12H-2, 70–71	100.80		3.63		30.2				
12H-4, 70–71	103.80	4.19	4.11	0.08	34.2	0.08	0.09	1.0	0.9
12H-6, 70–71	106.80		4.36		36.3				
13H-2, 70–71	110.30		2.86		23.8				
13H-4, 70–71	113.30	3.09	2.93	0.16	24.4	0.08	0.10	2.0	1.7
14H-2, 70–71	117.30		4.22		35.2				
14H-4, 70–71	120.30	5.56	5.23	0.33	43.6	0.08	0.19	4.0	1.8
14H-6, 70–71	123.30		3.54		29.5				
15H-2, 70–71	126.80		2.86		23.8				
15H-4, 70–71	129.80	2.82	2.43	0.39	20.2	0.10	0.42	3.8	0.9
16H-2, 70–71	135.80	3.88	3.58	0.30	29.8	0.08	0.31	3.8	1.0
16H-4, 70–71	138.80	5.92	5.46	0.46	45.5	0.09	0.11	5.2	4.1
16H-6, 70–71	141.80	3.89	3.55	0.34	29.6	0.09	0.18	3.8	1.8
17H-2, 70–71	145.30	5.64	5.47	0.17	45.6	0.07	0.00	2.4	
17H-4, 70–71	148.30	4.38	4.03	0.35	33.6	0.08	0.09	4.4	3.9
17H-6, 60–61	151.20	4.95	4.57	0.38	38.1	0.09	0.07	4.3	5.4
18H-2, 70–71	153.70	4.01	3.83	0.18	31.9	0.07	0.10	2.5	1.8
19H-2, 70–71	158.29	5.14	4.48	0.66	37.3	0.11	0.25	6.1	2.7
19H-4, 70–71	161.29	4.47	4.28	0.19	35.7	0.07	0.10	2.7	1.9
20H-1, 125–127	163.75	3.82	2.90	0.92	24.2	0.13	1.31	7.4	0.7
20H-2, 70–71	164.70	4.54	4.38	0.16	36.5	0.08	0.21	2.1	0.8
20H-3, 70–72	166.20	3.91	2.78	1.13	23.2	0.13	3.90	9.0	0.3
20H-4, 70–71	167.70	3.60	3.40	0.20	28.3	0.08	0.15	2.4	1.3
20H-5, 70–72	169.20	3.91	2.47	1.44	20.6	0.15	2.86	9.7	0.5
21H-2, 45–46	172.45	3.99	2.77	1.22	23.1	0.13	1.95	9.1	0.6
21H-2, 70–71	172.70	3.44	2.40	1.04	20.0	0.14	1.34	7.7	0.8
21H-4, 71–72	175.61	3.24	3.09	0.15	25.7	0.08	0.17	2.0	0.9
22H-1, 15–16	176.65	3.43	2.70	0.73	22.5	0.12	0.81	6.2	0.9
22H-2, 8–9	178.08	3.41	2.70	0.71	22.5	0.12	0.72	5.9	1.0
22H-2, 70–71	178.70	3.87	3.46	0.41	28.8	0.09	0.40	4.6	1.0
22H-4, 70–71	181.70	3.72	3.51	0.21	29.2	0.07	0.16	2.9	1.3
22H-6, 70–71	184.70	4.10	3.85	0.25	32.1	0.08	0.23	3.1	1.1
23H-1, 17–19	186.17	3.68	3.05	0.63	25.4	0.10	0.76	6.6	0.8
23H-1, 40–41	186.40	3.95	3.15	0.80	26.2	0.12	0.60	6.8	1.3
23H-2, 71–72	188.21	4.04	3.85	0.19	32.1	0.07	0.12	2.6	1.5
23H-4, 71–72	191.21	5.25	4.83	0.42	40.2	0.09	0.26	4.7	1.6
24H-2, 70–71	194.20	4.72	4.43	0.29	36.9	0.09	0.23	3.4	1.3
24H-4, 66–67	197.16	4.77	4.29	0.48	35.7	0.09	0.62	5.3	0.8
25H-1, 129–131	198.79	3.81	3.39	0.42	28.2	0.09	0.18	4.7	2.3
160-963B-									
14H-5, 115–116	124.05	3.62	3.21	0.41	26.74	0.09	0.20	4.5	2.0
14H-5, 147–148	124.37	5.51	4.02	1.49	33.49	0.15	1.03	9.9	1.4
19H-2, 10–11	160.00	4.73	3.94	0.79	32.82	0.11	0.61	7.3	1.3
19H-2, 30–31	160.20	3.36	2.33	1.03	19.41	0.13	15.20	7.9	0.1
19H-2, 73–74	160.63	3.99	3.24	0.75	26.99	0.10	0.79	7.2	0.9
19H-2, 90–91	160.80	3.65	3.32	0.33	27.66	0.08	0.56	4.2	0.6
19H-3, 73–74	162.13	4.42	3.27	1.15	27.24	0.13	1.40	8.8	0.8
19H-3, 90–91	162.30	4.08	3.03	1.05	25.24	0.11	0.76	9.4	1.4
19H-4, 107–108	163.97	4.13	3.24	0.89	26.99	0.12	0.81	7.4	1.1
19H-4, 116–117	164.06	3.41	3.10	0.31	25.82	0.08	0.12	3.9	2.6
20H-1, 89–90	166.29	4.13	2.89	1.24	24.07	0.14	0.14	8.9	8.9
20H-1, 110–111	166.50	4.41	4.04	0.37	33.65	0.16	0.64	2.3	0.6
20H-3, 60–61	169.00	3.20	2.54	0.66	21.16	0.11	0.86	6.0	0.8
20H-3, 76–77	169.16	3.71	2.53	1.18	21.07	0.14	2.02	8.4	0.6
20H-3, 96–97	169.36	3.86	2.53	1.33	21.07	0.14	2.07	9.5	0.6
20H-3, 117–118	169.57	3.83	2.68	1.15	22.32	0.15	1.52	7.8	0.8
20H-3, 144–145	169.84	3.68	3.35	0.33	27.91	0.09	0.17	3.8	1.9
21H-2, 119–120	177.59	3.77	2.65	1.12	22.07	0.13	1.11	8.6	1.0
21H-2, 145–146	177.85	3.64	3.31	0.33	27.57	0.09	0.10	3.7	3.3
21H-3, 107–108	178.97	3.59	2.66	0.93	22.16	0.13	0.86	7.2	1.1
21H-3, 125–126	179.15	3.21	2.86	0.35	23.82	0.10	0.17	3.5	2.1
22H-2, 47–48	185.37	4.22	3.11	1.11	25.91	0.13	0.91	8.5	1.2
22H-2, 80–81	185.70	4.60	3.38	1.22	28.16	0.11		11.1	
22H-2, 117–118	186.07	4.92	4.59	0.33	38.23	0.07	0.58	4.7	0.6
22H-4, 44–45	188.34	3.51	2.79	0.72	23.24	0.12	0.96	5.8	0.8
22H-4, 79–80	188.69	3.87	3.44	0.43	28.66	0.10	0.19	4.2	2.2
23H-2, 11–12	191.51	3.37	2.61	0.76	21.74	0.12	1.12	6.2	0.7
23H-2, 37–38	191.77	3.77	2.52	1.25	20.99	0.14	1.97	8.7	0.6
23H-2, 52–53	191.92	3.50	2.31	1.19	19.24	0.14	1.41	8.5	0.8
23H-2, 75–76	192.15	3.72	2.75	0.97	22.91	0.13	1.32	7.6	0.7
23H-2, 88–89	192.28	4.49	4.07	0.42	33.90	0.09	0.17	4.6	2.5
24H-1, 42–43	197.92	4.16	3.61	0.55	30.07	0.09	0.17	5.8	3.3
24H-1, 75–76	198.25	4.05	3.22	0.83	26.82	0.12	1.18	7.0	0.7
24H-1, 96–97	198.46	4.15	3.47	0.68	28.91	0.10	0.43	6.5	1.6
24H-1, 124–125	198.74	3.95	3.72	0.23	30.99	0.07	0.28	3.3	0.8
24H-2, 40–41	199.40	4.69	4.54	0.15	37.82	0.08	0.09	1.9	1.7
24H-2, 74–75	199.74	3.72	2.56	1.16	21.32	0.14	1.70	8.4	0.7
24H-2, 90–91	199.90	3.57	2.34	1.23	19.49	0.15	2.40	8.3	0.5
24H-2, 108–109	200.08	5.16	4.88	0.28	40.65	0.07	0.07	4.1	4.1

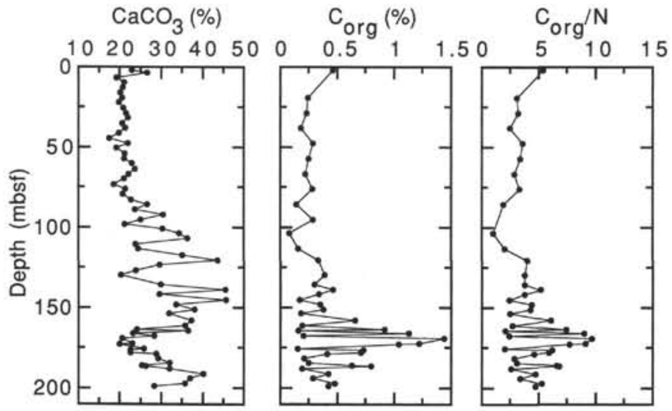

Figure 29. Downhole distribution of calcium carbonate and organic carbon concentrations and the ratio of organic carbon to total nitrogen in sediments at Hole 963A.

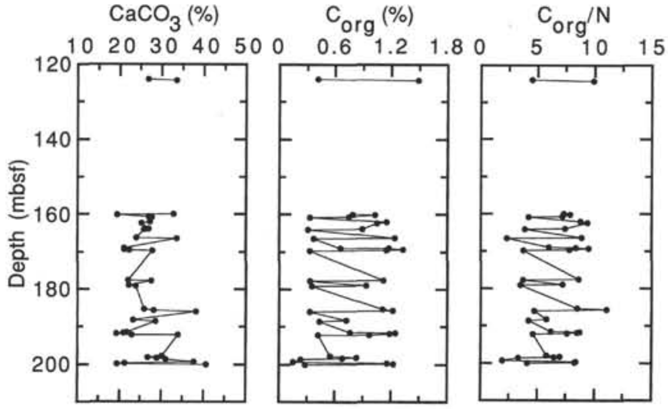

Figure 30. Downhole distribution of calcium carbonate and organic carbon concentrations and the ratio of organic carbon to total nitrogen in sediments at Hole 963B (Cores 160-963B-14H through 24H).

Table 12. Results of Rock-Eval analysis for Site 963.

Core, section, interval (cm)	Depth (mbsf)	S_1 (mg/g)	S_2 (mg/g)	S_3 (mg/g)	TOC (%)	PC	HI	OI	T_{max} (°C)	PI	S_2/S_3
160-693A-											
20H-1, 125–127	163.75	0.17	0.98	1.89	0.92	0.09	107	205	418	0.15	0.51
20H-3, 70–72	166.20	0.24	1.11	1.93	1.13	0.11	98	171	412	0.18	0.57
20H-5, 70–72	169.20	0.35	2.06	2.30	1.44	0.20	143	160	418	0.15	0.89
21H-2, 45–46	172.45	0.42	1.98	2.09	1.22	0.20	162	171	421	0.17	0.94
22H-1, 15–16	176.65	0.20	0.70	2.09	0.73	0.07	96	286	413	0.22	0.33
22H-2, 8–9	178.08	0.21	0.88	1.97	0.71	0.09	124	277	416	0.19	0.44
23H-1, 17–19	186.17	0.10	0.47	2.08	0.63	0.04	75	330	409	0.18	0.22
160-693B-											
14H-5, 147–148	124.37	0.52	2.45	3.09	1.49	0.24	164	207	416	0.18	0.79
19H-2, 30–31	160.20	0.20	0.82	1.99	1.03	0.08	79	193	412	0.20	0.41
19H-3, 73–74	162.13	0.28	1.39	2.71	1.15	0.13	120	235	418	0.17	0.51
19H-3, 90–91	162.30	0.12	0.43	2.43	1.10	0.04	39	220	406	0.22	0.18
20H-3, 76–77	169.16	0.36	1.39	2.84	1.20	0.14	115	236	403	0.21	0.49
20H-3, 96–97	169.36	0.42	2.34	2.57	1.30	0.23	180	197	415	0.15	0.91
20H-3, 117–118	169.57	0.11	1.03	2.94	1.20	0.09	85	245	408	0.10	0.35
21H-2, 119–120	177.59	0.15	0.75	2.20	1.10	0.07	68	200	409	0.17	0.34
22H-2, 47–48	185.37	0.31	1.55	2.36	1.10	0.15	140	214	414	0.17	0.66
22H-2, 80–81	185.70	0.21	0.56	2.45	1.20	0.06	46	204	398	0.28	0.23
23H-2, 37–38	191.77	0.36	2.14	2.14	1.30	0.20	164	164	419	0.14	1.00

Notes: TOC = total organic carbon; PC = petroleum potential as pyrolyzable carbon; HI = hydrogen index; OI = oxygen index; PI = production index; see the "Explanatory Notes" chapter (this volume) for units for these parameters.

Table 13. Index properties measured in cores from Hole 963A.

Core, section, interval (cm)	Depth (mbsf)	Water content (wt%)	Porosity (vol%)	Bulk density (g/cm^3)		Grain density (g/cm^3)		Dry density (g/cm^3)	
				Method B	Method C	Method B	Method C	Method B	Method C
160-963A-									
2H-1, 20–22	4.70	43.60	77.40	1.81	1.62	4.47	2.97	1.02	0.92
2H-2, 20–22	6.20	43.20	76.20	1.72	1.64	3.53	3.01	0.97	0.93
2H-3, 20–22	7.70	41.80	71.80	1.88	1.63	4.66	2.82	1.09	0.95
2H-4, 20–22	9.20	41.60	71.20	1.59	1.63	2.60	2.83	0.93	0.95
2H-5, 20–22	10.70	40.70	68.50	1.73	1.66	3.30	2.89	1.03	0.98
2H-6, 20–22	12.20	39.80	66.10	1.74	1.65	3.24	2.76	1.05	0.99
3H-1, 20–22	14.20	38.40	62.20	1.80	1.71	3.41	2.91	1.11	1.05
3H-2, 20–22	15.70	38.10	61.70	1.20	1.67	1.34	2.75	0.74	1.04
3H-3, 20–22	17.20	37.80	60.80	1.29	1.68	1.53	2.75	0.80	1.05
3H-4, 20–22	18.70	37.30	59.50	1.94	1.77	4.17	3.12	1.22	1.11

Only part of this table is reproduced here. The entire table appears on the CD-ROM (back pocket).

Table 14. Compressional wave velocity measured in cores from Hole 963A.

Core, section, interval (cm)	Depth (mbsf)	Measurement type	Velocity (km/s)
160-963A-			
1H-1, 135.2	1.35	DSV 1	1.501
1H-1, 135.5	1.36	DSV 2	1.51
1H-2, 187.8	3.38	DSV 1	1.497
1H-2, 188.7	3.39	DSV 2	1.504
1H-3, 187.1	4.87	DSV 2	1.503
1H-3, 188	4.88	DSV 1	1.516
2H-1, 177.9	6.28	DSV 1	1.507
2H-1, 177.9	6.28	DSV 2	1.51
2H-2, 141.3	7.41	DSV 1	1.508
2H-2, 141.7	7.42	DSV 2	1.514

Note: Direct DSV measurements.

Only part of this table is reproduced here. The entire table appears on the CD-ROM (back pocket).

Table 15. Vane shear strength measured in cores from Hole 963A.

Core, section, interval (cm)	Depth (mbsf)	Strength (kPa)
160-963A-		
1H-1, 205.4	2.05	10.6
1H-2, 185.9	3.36	22.9
1H-3, 187.5	4.88	24.7
2H-1, 177.9	6.28	27.3
2H-2, 140.3	7.40	35.3
2H-3, 162.3	9.12	46.7
2H-4, 152	10.52	46.9
2H-5, 132.3	11.82	54.4
2H-6, 142.8	13.43	59.5
3H-1, 172.7	15.73	63.6

Only part of this table is reproduced here.The entire table appears on the CD-ROM (back pocket).

Table 16. Thermal conductivity measured in cores from Hole 963A.

Core, section, interval (cm)	Depth (mbsf)	Thermal conductivity (W/[m · K])
160-963A-		
1H-2, 50	2.00	1.12
1H-2, 50	2.00	1.19
1H-2, 100	2.50	1.11
2H-2, 50	6.50	1.13
2H-5, 50	11.00	1.16
3H-2, 50	16.00	1.16
3H-6, 50	22.00	1.42
4H-2, 50	25.50	1.23
4H-5, 50	30.00	1.21
5H-2, 50	35.00	1.16

Only part of this table is reproduced here. The entire table appears on the CD-ROM (back pocket).

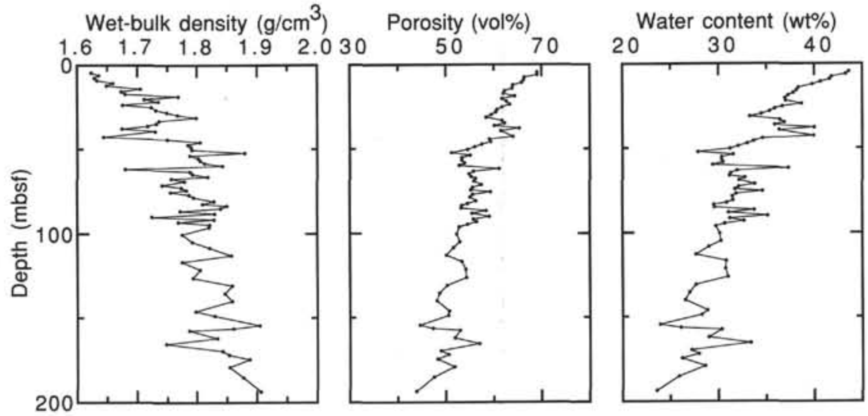

Figure 31. Index properties measured in cores from Hole 963A.

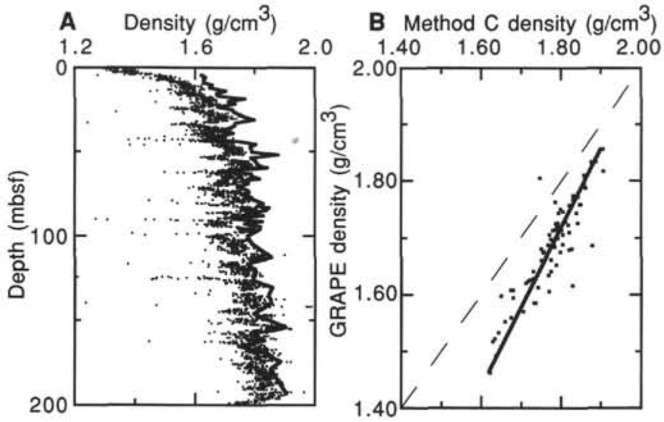

Figure 32. **A.** Density measured using the GRAPE instrument on the MST in comparison with index properties results (line). **B.** Linear regression (line) of index properties density with GRAPE density (points). The dashed line indicates a perfect correspondence between the two measurements and is for reference only. The correlation coefficient is R = 0.89.

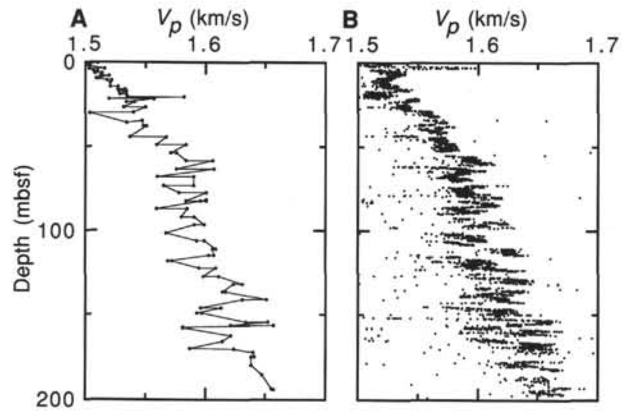

Figure 33. Compressional wave velocity measured in cores from Hole 963A. **A.** Direct measurements in split core sections with the DSV. **B.** MST measurements through the liner of whole core sections.

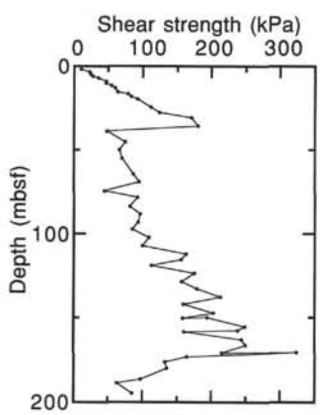

Figure 34. Vane shear strength measured in cores from Hole 963A.

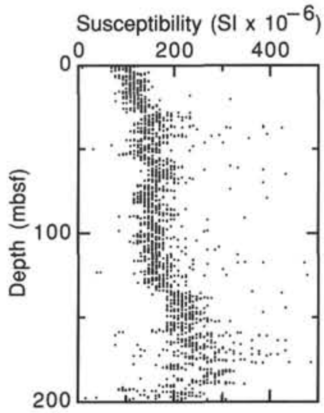

Figure 35. Magnetic susceptibility measured on the MST in cores from Hole 963A.

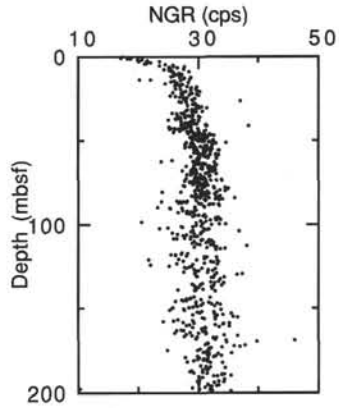

Figure 36. Natural gamma-ray radiation measured on the MST in cores from Hole 963A.

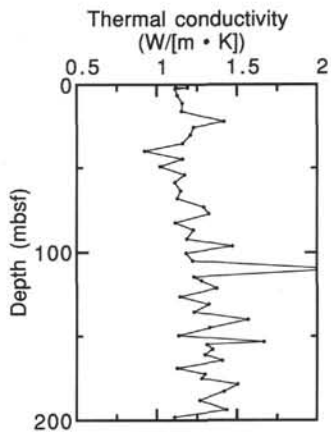

Figure 37. Thermal conductivity measured in cores from Hole 963A.